

# Bias Corrected Estimation of Paleointensity (BiCEP): An improved methodology for obtaining paleointensity estimates

Brendan J Cych<sup>1,1</sup>, Matthias Morzfeld<sup>2,2</sup>, and Lisa Tauxe<sup>3,3</sup>

<sup>1</sup>Scripps Institution of Oceanography

<sup>2</sup>UCSD

<sup>3</sup>University of California, San Diego

November 30, 2022

## Abstract

The assumptions of paleointensity experiments are violated in many natural and archaeological materials, leading to Arai plots which do not appear linear and yield inaccurate paleointensity estimates, leading to bias in the result. Recently, paleomagnetists have adopted sets of “selection criteria” that exclude specimens with non linear Arai plots from the analysis, but there is little consensus in the paleomagnetic community on which set to use. In this paper, we present a statistical method we call Bias Corrected Estimation of Paleointensity (BiCEP), which assumes that the paleointensity recorded by each specimen is biased away from a true answer by an amount that is dependent a single metric of nonlinearity (the curvature parameter  $\vec{k}$ ) on the Arai plot. We can use this empirical relationship to estimate the recorded paleointensity for a specimen where  $\vec{k}=0$ , i.e., a perfectly straight line. We apply the BiCEP method to a collection of 30 sites for which the true value of the original field is well constrained. Our method returns accurate estimates of paleointensity, with a higher level of accuracy and precision than the strict CCRIT selection criteria, and with higher accuracy and similar precision to the modified PICRIT03 criteria. The BiCEP method has a significant advantage over using these selection criteria because it achieves these accurate results without excluding large numbers of specimens from the analysis.

1 **Bias Corrected Estimation of Paleointensity (BiCEP):**  
2 **An improved methodology for obtaining paleointensity**  
3 **estimates**

4 **Brendan Cych<sup>1</sup>, Matthias Morzfeld<sup>1</sup>, Lisa Tauxe<sup>1</sup>**

5 <sup>1</sup>University of California, San Diego

6 **Key Points:**

- 7 • Empirical evidence suggests that paleointensity estimates for non-ideal specimens  
8 are biased.
- 9 • BiCEP is a method for estimating paleointensity for ensembles of specimens, cor-  
10 recting for bias
- 11 • BiCEP produces accurate results when applied to data where the true field strength  
12 is known.

---

Corresponding author: Brendan Cych, [bcych@ucsd.edu](mailto:bcych@ucsd.edu)

## 13 Abstract

14 The assumptions of paleointensity experiments are violated in many natural and archae-  
 15 ological materials, leading to Arai plots which do not appear linear and yield inaccurate  
 16 paleointensity estimates, leading to bias in the result. Recently, paleomagnetists have  
 17 adopted sets of “selection criteria” that exclude specimens with non linear Arai plots from  
 18 the analysis, but there is little consensus in the paleomagnetic community on which set  
 19 to use. In this paper, we present a statistical method we call Bias Corrected Estimation  
 20 of Paleointensity (BiCEP), which assumes that the paleointensity recorded by each spec-  
 21 imen is biased away from a true answer by an amount that is dependent a single met-  
 22 ric of nonlinearity (the curvature parameter  $\vec{k}$ ) on the Arai plot. We can use this em-  
 23 pirical relationship to estimate the recorded paleointensity for a specimen where  $\vec{k} =$   
 24 0, i.e., a perfectly straight line. We apply the BiCEP method to a collection of 30 sites  
 25 for which the true value of the original field is well constrained. Our method returns ac-  
 26 curate estimates of paleointensity, with similar levels of accuracy and precision to restric-  
 27 tive sets of paleointensity criteria, but accepting as many sites as permissive criteria. The  
 28 BiCEP method has a significant advantage over using these selection criteria because it  
 29 achieves these accurate results without excluding large numbers of specimens from the  
 30 analysis. It yields accurate, albeit imprecise estimates from sites whose specimens all fail  
 31 traditional criteria. BiCEP combines the accuracy of the strictest selection criteria with  
 32 the low failure rates of the less reliable ‘loose’ criteria.

## 33 Plain Language Summary

34 Paleomagnetists perform experiments on rocks and pottery sherds (among other  
 35 things) to estimate the strength of the ancient Earth’s magnetic field (the paleointen-  
 36 sity) through time. These make assumptions that are frequently violated, leading to bias.  
 37 Quantitative metrics (selection criteria) attempt to screen out ‘bad’ data. If a partic-  
 38 ular experiment fails the criteria, the results are ignored. However, there is a lack of agree-  
 39 ment as to which set of criteria are the most important and what is considered a fail-  
 40 ure. One of these criteria quantifies the deviation from the fundamental assumption of  
 41 linearity between the ancient and laboratory magnetizations. We present a new Bayesian  
 42 method called Bias Corrected Estimation of Paleointensity (BiCEP), in which we assume  
 43 that the estimated paleointensity depends on this deviation. We can then use this de-  
 44 pendency to correct the paleointensity made on an ensemble of specimens with differ-  
 45 ing deviations from ideal behavior. BiCEP allows us to calculate accurate estimates of  
 46 the ancient magnetic field, without ignoring results from non-ideal specimens. We test  
 47 BiCEP on paleomagnetic data for which the original field strength is well constrained.  
 48 BiCEP recovers the field strength with similar accuracy to stricter sets of criteria, but  
 49 gets results for a greater number of sites.

## 50 1 Introduction

51 Estimates of the strength of the ancient Earth’s magnetic field are currently made  
 52 by performing experiments that compare the natural remanent magnetization (NRM)  
 53 acquired by a specimen while cooling in the Earth’s field, to a remanence known as ther-  
 54 mal remanent magnetization (TRM) acquired by the specimen while cooling in a known  
 55 laboratory field. Such experiments include the Königsberger-Thellier-Thellier (KTT) fam-  
 56 ily of experiments (Königsberger, 1938; Thellier & Thellier, 1959), the Shaw family of  
 57 experiments (Shaw, 1974), and the multi-specimen family of experiments (Hoffman et  
 58 al., 1989), among others. All of these experimental families make assumptions about the  
 59 relationship between the magnetic field and the remanent magnetization which may or  
 60 may not be applicable (see the review by Tauxe & Yamazaki, 2015). In this paper, we  
 61 will focus on the KTT family of experiments.

62 KTT type experiments involve a double heating protocol in which a specimen is  
 63 heated two or more times to a series of temperatures up to the Curie Temperature. At  
 64 each temperature, the specimen is cooled in two different fields. This has the effect of  
 65 replacing the NRM with a TRM acquired in a known laboratory field. Data from KTT-  
 66 type experiments are normally represented by the Arai diagram (Nagata et al., 1963),  
 67 which plots the NRM magnetization remaining at each temperature step against the mag-  
 68 netization imparted in the laboratory (often referred to as partial TRM or pTRM). The  
 69 ratio of these two magnetizations, as represented by the slope of the best fitting line to  
 70 the Arai plot data, is generally taken to be the ratio of the two magnetizing fields (an-  
 71 cient,  $B_{anc}$  and laboratory,  $B_{lab}$ ).

72 KTT-type experiments rely on several assumptions which are frequently violated  
 73 in paleointensity experiments. These include thermochemical alteration of specimens which  
 74 may lead to the production of new magnetic minerals, and an assumption known as reci-  
 75 procity, which requires that the blocking temperature (the temperature below which grains  
 76 retain their magnetization after an external field is removed) is the same as the unblock-  
 77 ing temperature (the temperature above which grains equilibrate with the external field).

78 The reciprocity assumption of Thellier and Thellier (1959) is fundamental to Néel's  
 79 theory for uniaxial single domain grains (Néel, 1949). Néel theory assumes that the elec-  
 80 tronic spins within magnetic grains are fully aligned, and that the alignment is in one  
 81 of two directions along an energetically favorable 'easy' axis. In zero field, there is no pref-  
 82 erence for either direction, but in the presence of a field there is a slight preference for  
 83 the direction along the easy axis with the smallest angle to the applied field. If the reci-  
 84 procity assumption is met, then the energy required for the magnetization to change di-  
 85 rections along the easy axis is always the same regardless of whether the specimen is cooled  
 86 from higher temperature (blocking) or heated from room temperature (unblocking) and  
 87 the two temperatures are identical.

88 By assuming that electronic spins within magnetic grains are fully aligned, Néel  
 89 theory fails to take into account a term in the magnetic energy of grains which causes  
 90 deviations from full alignment, resulting in structures such as the vortex state of, e.g.,  
 91 Williams and Dunlop (1989). Although this effect is present in nearly all magnetic grains,  
 92 it is insignificant over short length scales (10s of nm) and so uniaxial single domain the-  
 93 ory may be a reasonable approximation for smaller, elongate grains. Specimens in pa-  
 94 leointensity experiments contain mixtures of grains with different sizes and shapes and  
 95 a specimen used for paleointensity is likely to include grains for which the applicability  
 96 of single domain theory does not hold.

97 Failure of reciprocity and other fundamental assumptions embedded in the KTT  
 98 family of experiments (laid out by e.g., Thellier & Thellier, 1959) provides a challenge  
 99 for those analyzing paleointensity data. Paleomagnetists generally use a set of selection  
 100 criteria which reject an intensity result if the NRM and pTRM data behave in a way which  
 101 deviate from single domain theory (linear on the Arai plot, see Figure 1a) by more than  
 102 some arbitrarily chosen threshold value. This is because data that contain a large pro-  
 103 portion of non single domain-like grains or which otherwise violate the assumptions of  
 104 the experiment are likely to give biased results (Tauxe et al., 2021). Selection criteria  
 105 generally operate in a binary way, with specimens either being 'accepted' or 'rejected'  
 106 from the estimation of the site mean, where 'site' is the collection of specimens assumed  
 107 to have cooled in identical external magnetic fields (say, a lava flow or ceramic fragment).

108 Figure 1 gives a demonstration of biased results in specimens from prepared mag-  
 109 netite powders of increasing grain size that were magnetized in a  $60 \mu\text{T}$  field (Krása et  
 110 al., 2003). If all assumptions of Thellier and Thellier (1959) were obeyed, we would ex-  
 111 pect the best fitting lines to data on Arai plots to give a range of values distributed closely  
 112 about a mean of  $60 \mu\text{T}$ . As the grain size of the powder increases, the Arai plot becomes  
 113 more curved and the best fitting line to the Arai plot yields a progressively lower inten-

114 sity estimate. As all the paleointensities estimated from the curved plots are below the  
 115 expected value, the estimate for the ensemble can be biased, with the high temperature  
 116 segment having an even lower mean value, and the low temperature segment having a  
 117 high mean value. The data of Tauxe et al. (2021) also demonstrate downward curved  
 118 Arai plots in natural samples are biased so this problem may effect many of the results  
 119 compiled in paleointensity databases like the MagIC database (Tauxe et al., 2016) or PINT  
 120 (Biggin, 2010).

121 The curvature of an Arai plot can be quantified using the curvature criterion ( $\vec{k}$ )  
 122 of Paterson (2011) (see also Paterson et al., 2014). Curvature is calculated using the re-  
 123 ciprocal of the radius of a circle fit to scaled Arai plot data (see Section 2.2.1). While  
 124 there is no theoretical basis for a circular fit (as opposed to the linear fit, which is firmly  
 125 rooted in Néel theory), it is a useful approximation that we will exploit in this paper.

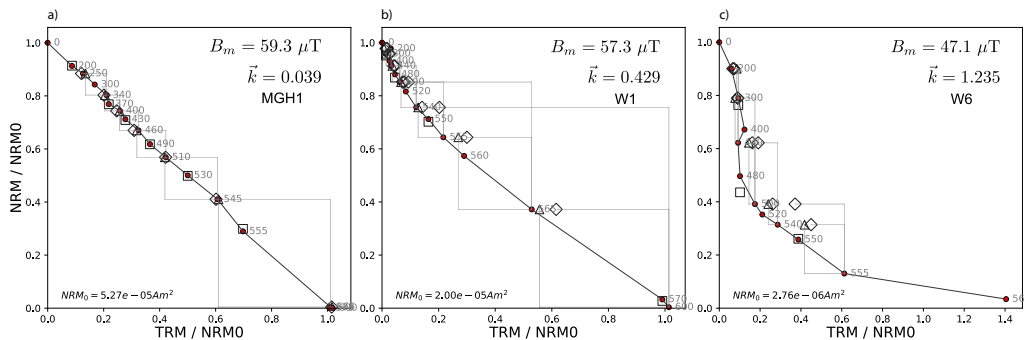


**Figure 1.** Arai plots from prepared magnetite powders given a TRM in a 60  $\mu\text{T}$  field (Krása et al., 2003). The curvature criterion,  $\vec{k}$  (Paterson, 2011) and specimen level paleointensity estimate  $B_m$  estimated from fitting a line to the entire Arai plot are plotted on the figure as text. The grain size of the magnetite powders increases from left to right. The coarser grains have non ideal domain state, leading to curved Arai plots and estimates of paleointensity which are biased to lower values than the expected 60  $\mu\text{T}$ . a) Nominal grain size of 23 nm. b) Mean grain size of 70 nm. c) Mean grain size of 12.1  $\mu\text{m}$ .

126 The practice of using binary (pass/fail) selection criteria is problematic for many  
 127 reasons. Paleomagnetic specimens generally contain magnetic carriers which span a range  
 128 of grain sizes and may or may not conform to the assumptions of the method. In addition,  
 129 micromagnetic simulations (e.g., Williams & Dunlop, 1989; Nagy et al., 2017) demon-  
 130 strate that the change in magnetic domain state with grain size is a continuum, and so  
 131 one individual grain’s behaviour may be more or less ideal than any other’s. With bi-  
 132 nary pass/fail criteria, the distinction between ‘good’ and ‘bad’ data must be assessed  
 133 with an arbitrary threshold value, which does not reflect the range of behaviors within  
 134 both groups. Consequently there are a large number of selection criteria in common use  
 135 (over 40 in Paterson et al., 2014), most of which have some empirical rationale, but there  
 136 is little agreement on which set to use or their threshold values.

137 In this paper, we describe a new approach for paleointensity estimation that treats  
 138 the quality of paleointensity data as a continuum as opposed to the binary ‘in’ or ‘out’  
 139 approach using selection criteria. We assume that paleointensities become more biased  
 140 as specimens’ magnetic behaviors become more non-ideal and their Arai plots become  
 141 less linear. By allowing the data interpretation for specimens to be based on the shape  
 142 of their Arai plots, we are able to obtain unbiased estimates of paleointensity without  
 143 the need for many specimen level (binary) selection criteria. We call this method the ‘Bias

Corrected Estimation of Paleointensity' or BiCEP. In the next section, we develop a Bayesian approach to obtain accurate paleointensity estimates with realistic uncertainties, using  $\vec{k}$  as a metric of bias, and show how to combine data at the site level. In Section 3 we compare results from the BiCEP method to those of more traditional selection criteria based approaches. We discuss the results in Section 4 and summarize our conclusions in Section 5. Accompanying this paper, we release a Graphical User Interface (GUI) which can apply the BiCEP method to MagIC formatted data. Links and instructions on how to access the code can be found in Appendix 6.3.

## 2 Methods

### 2.1 Accounting for bias in paleointensity experiments

Paleomagnetists determine the paleointensity for a site by performing a Thellier-type double heating experiment on multiple specimens from that site. According to the theory for single domain grains (assuming no alteration of the specimen during heating), the ratio of NRM lost to pTRM gained is the ratio of the ancient field to the laboratory field. If the specimen conforms to theory, the Arai plot data will fall along a line the slope of which is equal to the ratio of ancient to the laboratory field (see Figure 1a).

We expect that the field strength predicted by the slope of the line on the Arai plot for each specimen (here called  $B_m$ ) will be distributed about the true (expected) ancient field ( $B_{exp}$ ) at the site with a Gaussian distribution. However, rarely do a set of specimens from a site all produce linear Arai plots that are easily interpretable. For example, interpretation of data from specimens with magnetic grains exhibiting non single domain magnetic domain states produce non-linear Arai plots which violate the assumptions of the method (e.g., Dunlop & Özdemir, 2001). Fitting lines to the data on such Arai plots often produces estimates of paleointensity which are biased (see Figure 1c, Krása et al., 2003), which in turn would bias site level estimates.

Paleomagnetists generally approach non-ideal data by using certain quantitative criteria chosen to eliminate results suffering from one or more pathologies (Paterson et al., 2014). If a particular criterion calculated for a specimen fails to meet some threshold value, then the specimen is excluded from the analysis. In this paper, we present an alternative approach in which we allow for specimens to behave in a non-ideal (non-linear) fashion when considering how specimen intensity estimates are distributed about a site mean and weight the contribution of individual specimen estimates according to linearity. Under such a scheme, we start by predicting a bias for each specimen, and the specimens with the smallest predicted bias most strongly determine the paleointensity at that site. In this way, biased specimens do not strongly affect our site intensity estimate, as they are down-weighted, yet provide useful constraints on the uncertainty.

To predict the amount of bias a specimen is likely to have, we require a proxy for bias in paleointensity experiments. For this we use the curvature criterion  $\vec{k}$  of Paterson (2011) (see Section 2.2.1). There are several reasons that make this criterion a useful proxy for bias in paleointensity experiments:

- Specimens that are highly linear have, by definition, low values for  $|\vec{k}|$  and will generally give unbiased paleointensity estimates (e.g., Cromwell et al., 2015).
- By contrast, specimens with higher  $|\vec{k}|$  yield biased paleointensities, with the magnitude of the bias generally increasing with the magnitude of  $|\vec{k}|$  (e.g., Tauxe et al., 2021).
- $|\vec{k}|$  has an empirical correlation with magnetic grain size (Paterson, 2011).

Site	Citation	Material	Lat.	Long.	Year	$B_{exp}$	$M$
1991-1992 Eruption Site	Bowles et al. (2006)	lava flow	9.8	-104.3	1991	36.2	53
hw108	Cromwell et al. (2015)	lava flow	19.9	-155.9	1859	39.3	23
hw123	Cromwell et al. (2015)	lava flow	19.1	-155.7	1907	37.7	12
hw126	Cromwell et al. (2015)	lava flow	19.7	-155.5	1935	36.4	13
hw128	Cromwell et al. (2015)	lava flow	19.3	-155.9	1950	36.2	26
hw201	Cromwell et al. (2015)	lava flow	19.4	-155.0	1990	35.2	12
hw226	Cromwell et al. (2015)	lava flow	19.6	-155.5	1843	39.9	11
hw241	Cromwell et al. (2015)	lava flow	19.5	-155.8	1960	36.0	18
BR06	Donadini et al. (2007)	brick	60.1	24.9	1906	49.7	3
P	Muxworthy et al. (2011)	lava flow	19.3	-102.1	1943	44.6	36
VM	Muxworthy et al. (2011)	lava flow	40.8	14.5	1944	43.8	18
BBQ	Pick and Tauxe (1993)	submarine lava flow	9.8	-104.3	1990	36.2	12
rs25	Shaar et al. (2010)	synthetic	N/A	N/A	N/A	30.0	5
rs26	Shaar et al. (2010)	synthetic	N/A	N/A	N/A	60.0	5
rs27	Shaar et al. (2010)	synthetic	N/A	N/A	N/A	90.0	10
remag-rs61	Shaar et al. (2011)	synthetic	N/A	N/A	N/A	40.0	6
remag-rs62	Shaar et al. (2011)	synthetic	N/A	N/A	N/A	60.0	6
remag-rs63	Shaar et al. (2011)	synthetic	N/A	N/A	N/A	80.0	5
remag-rs78	Shaar et al. (2011)	synthetic	N/A	N/A	N/A	20.0	4
kf	Tanaka et al. (2012)	lava flow	65.7	-16.8	1984	52.0	3
Hawaii 1960 Flow	Yamamoto et al. (2003)	lava flow	19.5	-155.8	1960	36.0	22
SW	Yamamoto and Hoshi (2008)	lava flow	31.6	-130.6	1946	46.4	19
TS	Yamamoto and Hoshi (2008)	lava flow	31.6	-130.6	1914	47.8	53
ET1	Biggin et al. (2007)	basaltic lava	37.8	15.0	1950	43.3	3
ET2	Biggin et al. (2007)	basaltic lava	37.8	15.0	1979	44.1	2
ET3	Biggin et al. (2007)	basaltic lava	37.8	15.0	1983	44.2	4
Synthetic60	Krása et al. (2003)	synthetic	N/A	N/A	N/A	60.0	7
LV	Paterson et al. (2010)	Lithic Clasts	-23.4	67.7	1993	24.0	45
MSH	Paterson et al. (2010)	Lithic Clasts	46.2	-122.2	1980	55.6	19
FreshTRM	Santos and Tauxe (2019)	remagnetized/synthetic	N/A	N/A	N/A	70.0	24

**Table 1.** Table of sites used for analysis in this study, including original study locations, latitude, longitude and year of magnetization (where applicable), expected field at that location ( $B_{exp}$ ), number of specimens used for analysis at that site  $M$ . Lat.: site latitude ( $^{\circ}$ N). Long. site longitude ( $^{\circ}$ E. N/A: Not Applicable (Synthetic)).  $B_{exp}$  is either a known laboratory field, from the International Geomagnetic Reference Field (IGRF, Thébault et al., 2015 or in two cases (hw226,hw108) using the Arch3k.1 model of Korte et al., 2009

190 To predict bias, we can use a method by which we minimize the misfit to a model  
 191 assuming that  $B_m$  is linearly related to  $\vec{k}$  for all specimens. In other words, we say that:

$$B_m = B_{exp} + c\vec{k}_m + \epsilon \quad (1)$$

192 where  $m$  is an index reflecting the specimen number,  $\epsilon$  is an error term and  $B_{exp}$  is the  
 193 true value of  $B$ . Effectively, our model just becomes a linear fit between the specimen  
 194 estimate  $B_m$  and  $\vec{k}$ , the y-intercept of which is the true value of the field  $B_{exp}$  and  $c$  is  
 195 a slope constant. While there is no theoretical justification (yet) for why  $B_m$  would be  
 196 related to  $\vec{k}_m$ , although it has been observed empirically (by Paterson, 2011 using the  
 197 data in Figure 1, and more recently by Tauxe et al., 2021), a linear model is the simplest  
 198 one to relate the two. We demonstrate in Section 3.3 that more complex models with  
 199 a quadratic and cubic fit relating  $B_m$  to  $\vec{k}_m$  perform worse than the linear model when  
 200 predicting the paleointensity for sites for which the paleointensity is well constrained (his-  
 201 torical lava flows or laboratory remanences).

202 Arai plot curvature is not the sole cause of bias in paleointensity experiments. In  
 203 some cases, specimens with Arai plots which do not have high  $|\vec{k}|$  but are still non lin-  
 204 ear (e.g., ‘zig-zagged’ as in, e.g., Yu et al., 2004), may still cause bias in paleointensity  
 205 experiments. To counteract this, we use a Bayesian method of calculating  $\vec{k}_m$  and  $B_m$   
 206 which provides an uncertainty for both of these parameters. The benefit of this approach  
 207 is that specimens whose Arai plots are not well fit by a line or an elliptical arc have less  
 208 influence on the linear fit. Therefore, the specimens with the lowest uncertainty in  $\vec{k}$  are  
 209 generally the most linear, and will have the most influence on the linear fit. Yet, for each  
 210 specimen, there is a trade off between minimizing the circle fit at a specimen level and  
 211 the linear fit between  $B_m$  and  $\vec{k}$  for specimens from the same site, an issue we will deal  
 212 with in Section 2.2.3.

213 Figure 2 shows results from our method (detailed in Section 2.2) applied to sev-  
 214 eral sites for which the true value of  $B_{anc}$  (here,  $B_{exp}$ ) is either calculated from the In-  
 215 ternational Geomagnetic Reference Field (IGRF, Thébault et al., 2015) or Arch3k.1 (Korte  
 216 et al., 2009) for historical flows, or known as the NRM is a laboratory TRM imparted  
 217 to the specimens. Following Equation 1, the uncertainty in the intercept value of these  
 218 linear fits gives us the uncertainty for our site value of  $B_{anc}$ . In this way, we can obtain  
 219 an unbiased estimate of  $B_{anc}$  without relying on arbitrary binary (accept/reject) crite-  
 220 ria to exclude specimen results.

221 In the following, we detail how the specimen level circle fit  $\vec{k}$  and site level pale-  
 222 ointensity for unknown values for  $B$  (here called  $B_{anc}$ ) can be calculated. We then com-  
 223 pare the efficacy of several different versions of our model to classical selection criteria.  
 224 We do this using a data compilation from 30 sites updated from Paterson et al. (2014)  
 225 and Tauxe et al. (2016) for which  $B_{exp}$  is well constrained (see Table 1 for details con-  
 226 cerning the original publications of the data).

## 227 **2.2 Statistical Methodology**

### 228 **2.2.1 Estimating curvature**

229 Paterson (2011) proposed a least squares fit of circles in Arai plot data. The pa-  
 230 rameter  $\vec{k}$  of Paterson (2011) is defined as the reciprocal of the radius of a best-fitting  
 231 circle through the data. It is positive if the circle center is to the upper right of the Arai  
 232 plot data (concave up, Figure 3a) and negative if the circle center is below and to the  
 233 left of the Arai plot data (concave down, Figure 3b).

234 Before fitting to the Arai plot data, Paterson (2011) scales the pTRMs by the max-  
 235 imum pTRM to ensure that the paleointensity data are independent of the laboratory  
 236 field. For estimating  $\vec{k}$ , we also subtract the minimum remaining NRM ( $NRM_{min}$ ) for  
 237 specimens for which full demagnetization has not been completed and we subtract the

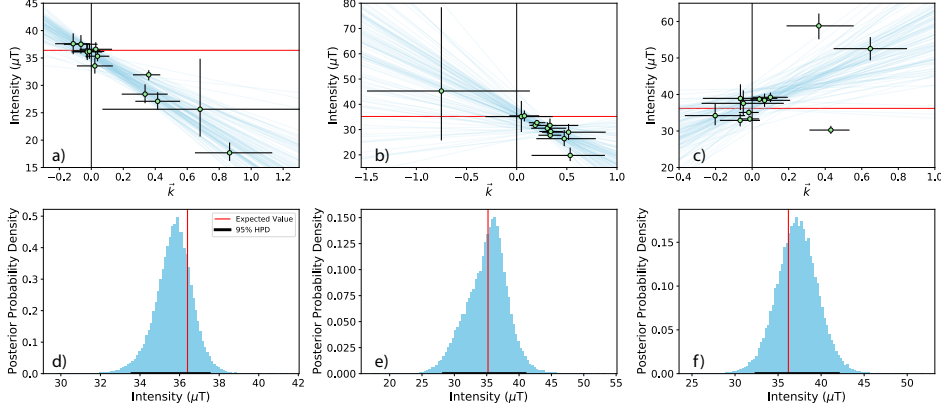


**Figure 2.** Example of results from the BiCEP method for several sites used as examples in this study. Lines (in blue) are fit to the values of  $B_m$  and  $\vec{k}$  for each specimen (blue dots, with uncertainties as black lines). The values of linear fits at  $\vec{k} = 0$  (blue histograms) provide an unbiased estimate of the expected paleointensity value at the site from the known field (red lines). a,d) hw126. b,e) hw201. c,f) BBQ. See Table 1 for sampling and citation details and Section 3 for comparison with the expected field values,  $B_{exp}$ .

238 minimum pTRM (pTRM<sub>min</sub>) for specimens for which the low temperature steps were  
 239 excluded from the analysis (e.g., because of viscous remanent magnetization).

240 For the BiCEP method, we define two sets of data vectors  $x$  and  $y$ :

$$x_n = \frac{\text{pTRM}_n - \text{pTRM}_{min}}{\text{pTRM}_{max}}, \quad y_n = \frac{\text{NRM}_n - \text{NRM}_{min}}{\text{NRM}_0}, \quad (2)$$

241 where  $n$  is the index of the data point. Because scaling should be by the total (original)  
 242 TRM (the NRM), we also exclude specimens whose  $\text{NRM}_{min}$  is more than 25% of the  
 243 initial NRM. This is justified by the assumption that the experimenter did not carry out  
 244 demagnetization to fully replace the NRM. Then, to fit a circle with center  $x_c, y_c$  and  
 245 radius  $R$  to the data, we try to minimize the squared perpendicular distance  $d_n^2$  (Fig-  
 246 ure 3a) of all the  $n$  data points to the circle edge:

$$\sum_{n=1}^N d_n^2 \quad \text{where} \quad d_n^2 = (\sqrt{(x_n - x_c)^2 + (y_n - y_c)^2} - R)^2. \quad (3)$$

247 In a total least squares fit, Equation 3 would be our objective function that we would  
 248 minimize. To fit circles to the Arai plot using a Bayesian method, we use Bayes' formula  
 249 (Equation 4). This formula allows us to assign a probability distribution to the values  
 250 of different parameters (in this case,  $\vec{k}_m$  and  $B_m$ ), rather than just finding the 'best' value  
 251 of the parameters. In a Bayesian context, we can simply assume that the data have some  
 252 Gaussian noise distribution with some unknown standard deviation  $\sigma$  and apply Bayes'  
 253 formula (e.g., Gelman et al., 2004):

$$P(\text{Parameters}|\text{Data}) = \frac{P(\text{Data}|\text{Parameters})P(\text{Parameters})}{P(\text{Data})}, \quad (4)$$

254 where the left hand side is the probability of the parameters given the data and the right  
 255 hand side is the probability of the data given the parameters times the probability of the

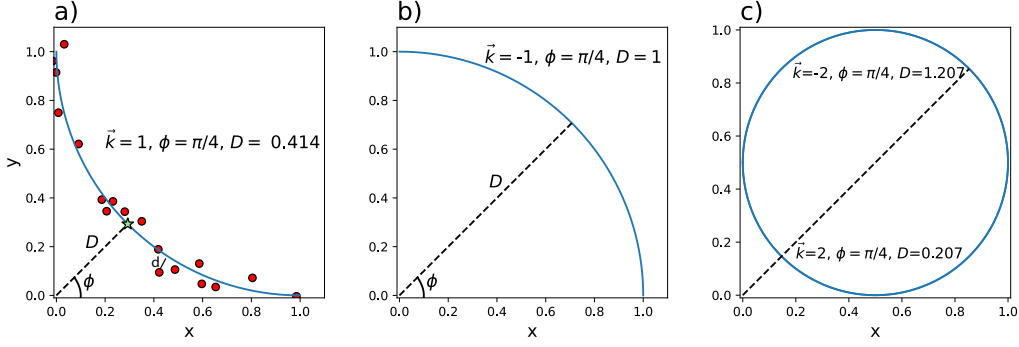


**Figure 3.** Example circles with different values for parameters  $\vec{k}$  and  $D$  with the same  $\phi$ , showing how these parameters define a circle. a) Positive  $\vec{k}$ . Red dots are example data, and the green star is the intersection of  $D, \phi$  with the circle edge (see text for definitions).  $d$  is the distance of an individual data point from the best-fit curve (blue). b) Negative  $\vec{k}$ . Note that in this case,  $\phi$  could take any value as the circle center is at the origin, making the definition of  $\phi$  meaningless in this case. c) Example showing how two sets of the parameters  $\vec{k}, \phi, D$  can describe the same circle.

256 parameters, normalized by the probability of the data. In our case, the parameters are  
 257  $x_c, y_c, R$  and  $\sigma$  and our data are  $x$  and  $y$  so we rewrite Equation 4 as:

$$P(x_c, y_c, R, \sigma | x, y) = \frac{P(x, y | x_c, y_c, R, \sigma) P(x_c, y_c, R, \sigma)}{P(x, y)}. \quad (5)$$

258 The term  $P(x, y | x_c, y_c, R, \sigma)$  is known as the “likelihood” and is based on the prob-  
 259 ability of generating the observed data from a given set of parameters using the assumed  
 260 Gaussian distribution. The term  $P(x_c, y_c, R, \sigma)$  is known as the “prior” and is a prob-  
 261 ability distribution for values of  $x_c, y_c, R$  and  $\sigma$  we consider to be reasonable before we  
 262 see any data. We consider the priors on these parameters to be independent of one an-  
 263 other, so we could rewrite this as  $P(x_c)P(y_c)P(R)P(\sigma)$ . The term  $P(x, y)$  is known as  
 264 the “evidence”, and is simply a normalizing constant that makes the “posterior” prob-  
 265 ability distribution,  $P(x_c, y_c, R, \sigma | x, y)$ , integrate to 1. In our application, we can sim-  
 266 plify the relationship by ignoring the normalization. Furthermore, we can say from the  
 267 definition of the Gaussian distribution that:

$$P(x, y | x_c, y_c, R, \sigma) = \left( \frac{1}{2\pi\sigma^2} \right)^{N/2} \exp \left( \sum_{n=1}^N -\frac{d_n^2}{\sigma^2} \right). \quad (6)$$

268 Now we have an expression for our posterior probability distribution:

$$P(x_c, y_c, R, \sigma | x, y) \propto \left( \frac{1}{2\pi\sigma^2} \right)^{N/2} \exp \left( \sum_{n=1}^N -\frac{d_n^2}{\sigma^2} \right) P(x_c, y_c, R) P(\sigma). \quad (7)$$

269 Because the actual noise distribution of the Arai plot data is quite complicated (Paterson  
 270 et al., 2012), we do not know the value of  $\sigma$ , so we use the uninformative prior  $P(\sigma) \propto$   
 271  $\frac{1}{\sigma}$ ; in other words, the smaller  $\sigma$ , the more likely the result. We can then substitute this  
 272 prior into Equation 7 and integrate out  $\sigma$  to obtain:

$$P(x_c, y_c, R | x, y) \propto \left( \sum_{n=1}^N d_n^2 \right)^{-N/2} P(R, x_c, y_c) \quad (8)$$

273 where  $N$  is the total number of measurements considered.

274 The set of parameters  $x_c, y_c$  and  $R$  is not easy to solve for, because Equation 3 has  
 275 multiple local minima (see Chernov and Lesort (2005) for a more detailed discussion).  
 276 Consider the simple case of a specimen with a linear Arai plot; in even this simplest case,  
 277 there are four minima, as both  $R$  and  $x_c, y_c$  will be either positive or negative and very  
 278 large. To avoid this complexity, we can use instead a change of parameters similar to that  
 279 of Chernov and Lesort (2005) which Paterson (2011) used as a basis for the circle fit-  
 280 ting protocol. Based on this, we define a set of three new parameters which avoid the  
 281 problem of multiple minima.

282 Firstly, we require a point on the Arai plot which can be related to a unimodal dis-  
 283 tribution. We know that linear data will plot along the edge of a circle (the tangent),  
 284 so if we draw a line from the origin toward the center  $(x_c, y_c)$  (not shown), this will touch  
 285 the edge of the circle at some distance  $D$  (green star in Figure 3a). The angle to the hor-  
 286 izontal of this line we call  $\phi$  and we can directly estimate the  $\vec{k}$  parameter of Paterson  
 287 (2011) using Equations 9,10,11. We can then establish equations for transforming be-  
 288 tween these two sets of parameters (see Appendix 6.1 for a more detailed derivation):

$$x_c = \left( D + \frac{1}{\vec{k}} \right) \cos(\phi), \quad (9)$$

$$y_c = \left( D + \frac{1}{\vec{k}} \right) \sin(\phi), \quad (10)$$

$$R = \frac{1}{|\vec{k}|}. \quad (11)$$

291 Despite this transformation, the circle fitting equation can still have multiple min-  
 292 ima, even with  $\vec{k}, D, \phi$  as our parameters, as the line connecting the origin to the hor-  
 293 izontal touches the circle edge in two locations (see Figure 3c). However, we can use prior  
 294 distributions to avoid this.

295 Chernov and Lesort (2005) define a function of the data  $d_{max}$  to define the region  
 296 of possible values for  $\vec{k}$ :

$$d_{max} = \max_{i,j} \sqrt{(x_i - x_j)^2 + (y_i - y_j)^2} \quad (12)$$

297 Additionally, we define distance from the origin to the centroid of the data,  $d_{cent}$ :

$$d_{cent} = \sqrt{\bar{x}^2 + \bar{y}^2} \quad (13)$$

298 Using this function, we can assume that  $D < 2d_{cent}$  and  $|\vec{k}| < N/d_{max}$  and can de-  
 299 fine priors for our parameters:

$$P(D) \sim \text{Uniform}(0, 2d_{cent}), \quad (14)$$

$$P(\phi) \sim \text{Uniform}(0, \pi), \quad (15)$$

301 and

$$P(\vec{k}) \sim \text{Uniform}(-N/d_{max}, N/d_{max}). \quad (16)$$

302 Using these priors gives us a posterior with a single maximum in most cases, which makes  
 303 the problem much easier to solve computationally.

304 We can now apply a Bayesian approach to estimate  $\vec{k}$  for all temperature steps for  
 305 a given specimen  $m$ . It is frequently useful to choose a subset of the temperature steps

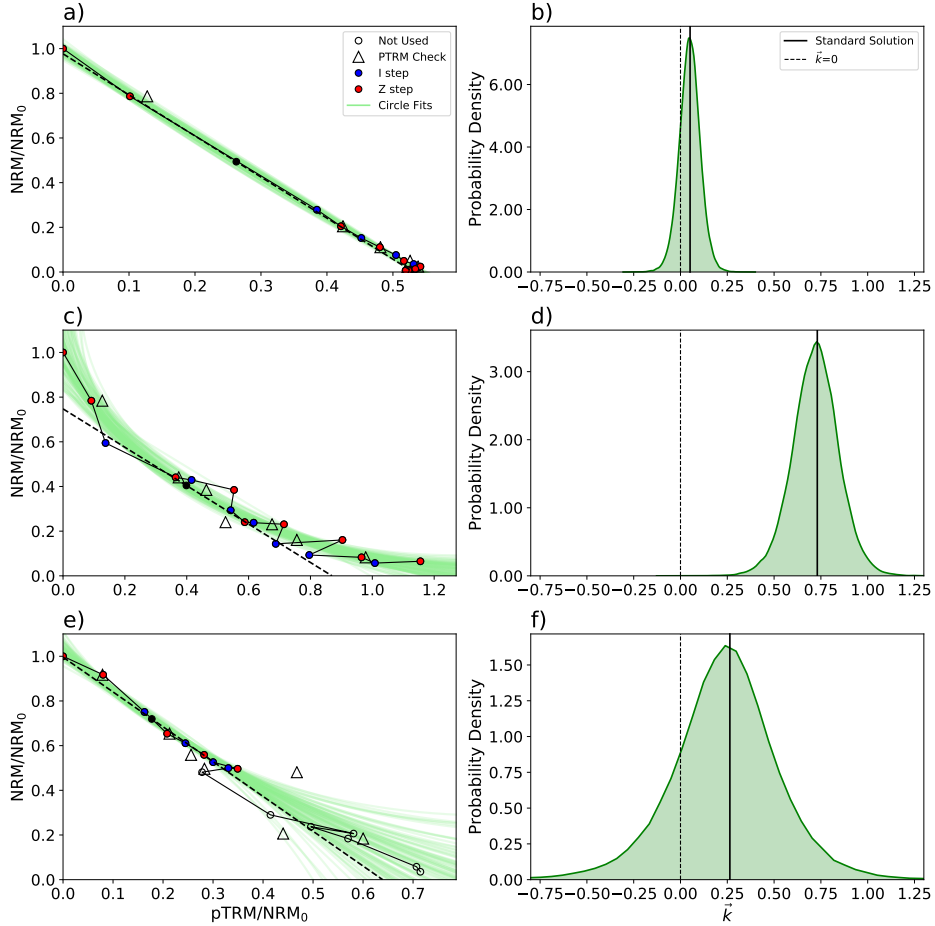


**Figure 4.** Examples of circle fits to Arai plots (left column) and approximate probability densities of  $\vec{k}$  (right column). Dashed lines in the left hand plots are the tangents to circles with the median values for  $\phi$  and  $D$ . We use tangents to the circle to get an estimate for  $B_m$  as outlined in Section 2.2.2. Triangles in a), c), e) are repeated lower temperature steps (pTRM checks) that indicate alteration of magnetic minerals during the experiment when offset from the original measurements (red dots). a) Specimen hw126a1. A fit to a straight line yields a precise  $\vec{k}$  distribution with a maximum close to zero (b). c) Specimen hw126a7. A curved Arai plot with a high amount of scatter/zigzagging (left) results in a higher uncertainty in the value of  $\vec{k}$  (d). e) Specimen hw126a6. Arai plot for a specimen that underwent thermochemical alteration at high temperature. A circle fit to just the low temperature steps results in a high uncertainty in the value of  $\vec{k}$  (f). Note that we do not exclude any measurements due to thermal alteration in our results section, and that this is only done here for illustrative purposes.

306 (e.g., if there is evidence for multiple components of the NRM or heating related alteration,  
 307 as detected by repeated lower temperature pTRM steps). When using a subset  
 308 of steps, we scale by the maximum pTRM for all temperature steps and the NRM at room  
 309 temperature; in this way we can predict the curvature for the part of the Arai plot that  
 310 is missing. This means that interpretations based on a small fraction of the Arai plot  
 311 will have large uncertainties in the value of  $\vec{k}$ . Therefore, our circle fit can prioritize in-  
 312 terpretations using the largest fraction of the NRM.

313 Figures 4a,c,e show circle fits sampled from the posterior distributions for speci-  
 314 mens from site hw126 (site level results shown in Figure 2a). The probability densities  
 315 of all the  $\vec{k}$  values for each specimen are plotted in Figures 4b,d,f. The plot demonstrates  
 316 how a straight Arai plot (Figure 4a) produces a narrow posterior about  $\vec{k} = 0$  (Figure 4b),  
 317 while a curved one (Figure 4c) produces a posterior which does not contain  $\vec{k} = 0$  (Fig-  
 318 ure 4d). In the example with failed pTRM checks at higher temperatures (offset trian-  
 319 gles in Figure 4e), we exclude the data points represented by open circles and use a lin-  
 320 ear segment with only a portion of the results, the posterior distribution of  $\vec{k}$  has a larger  
 321 uncertainty on the value, translating to a larger uncertainty in the bias for that spec-  
 322 imen. We do not advocate for any particular method of checking for alteration, and do  
 323 not exclude any measurement steps in our results section. However, our circle fitting rou-  
 324 tine allows for measurement steps to be excluded and accounts for the increased uncer-  
 325 tainty in doing so.

### 326 *2.2.2 Obtaining a specimen level paleointensity estimate*

327 Analogous to the case in which paleointensity estimates are made using the slope  
 328 of a fitted line to the Arai plot data, we can obtain a similar “slope” value for a circu-  
 329 lar arc fit to the data. Consider the case in which the edge of the circle forms an exact  
 330 line ( $\vec{k}=0$ , see Figure 4a). In this case, the slope of the line can be given by the tangent  
 331 to the circle at the point where it intersects a line drawn from the origin (0,0) to the cir-  
 332 cle center (Figure 3a). In other words, the “slope” of the Arai plot can be estimated as  
 333  $\cot \phi$ , which gives the tangent to the circle. We can then turn this into an intensity es-  
 334 timate  $B_m$  using the formula:

$$B_m = \frac{B_{lab} \cot(\phi)}{pTRM_{max}}, \quad (17)$$

335 where  $B_{lab}$  is the laboratory field used to impart a pTRM to the specimen. If a spec-  
 336 imen is corrected for anisotropy, cooling rate, or non-linear acquisition of TRM, we ap-  
 337 ply this correction to Equation 17.

338 We now have a way of obtaining estimates for  $B_m$  and  $\vec{k}_m$  for each specimen. We  
 339 use the methodology laid out in Sections 2.2.1 and 2.2.2 to plot the median value of the  
 340 posterior for these parameters (with error bars) in Figure 5a, and examples of circle fits  
 341 in Figures 5c, e, g. For specimens with values of  $\vec{k}$  that are approximately 0 (Figure 5g),  
 342 the  $B_m$  values are quite accurate. There appears to be a bias for specimens with large  
 343  $\vec{k}$ , with the amount of bias increasing as  $\vec{k}$  increases. In this example, large positive val-  
 344 ues of  $\vec{k}$  lead to a large underestimates of  $B_m$  while negative values of  $\vec{k}$  lead to overes-  
 345 timates of  $B_m$  (although small in this example).

### 346 *2.2.3 Obtaining a site level paleointensity estimate*

347 The main problem with the method presented thus far is that we still do not have  
 348 a way of obtaining an estimate for  $B_{anc}$ , the unknown value at the site level. However,  
 349 in Figure 5a there appears to be a dependence between  $\vec{k}_m$  and  $B_m$  as suggested ear-  
 350 lier, with most of the specimens showing a quasi-linear relationship (the only exception  
 351 being the point labeled e) whose Arai plot is shown in Figure 5e) and suggests there is  
 352 a great deal of uncertainty in the value of  $\vec{k}$  itself. Because of this, we can modify our  
 353 model slightly by imposing the extra restriction that  $B_m$  must be linearly dependent on  
 354  $\vec{k}_m$  (with noise) using Equation 1 (substituting  $B_{anc}$  for the unknown value of  $B_{exp}$ ).

355 Previous papers have assumed that  $B_{anc}$  for selected specimens follows a Gaussian  
 356 distribution and we can also make this assumption here. In the following, we will show  
 357 how this modification can shift results from specimens that are offset from the linear re-  
 358 lationship toward the line (as in the point labeled ‘f’ in Figure 5b) and produce mod-

359  
360

els (shown as blue lines) that estimate all of our  $B_m$ . We can then use the resulting models to estimate the probability distribution for  $B_m$  as:

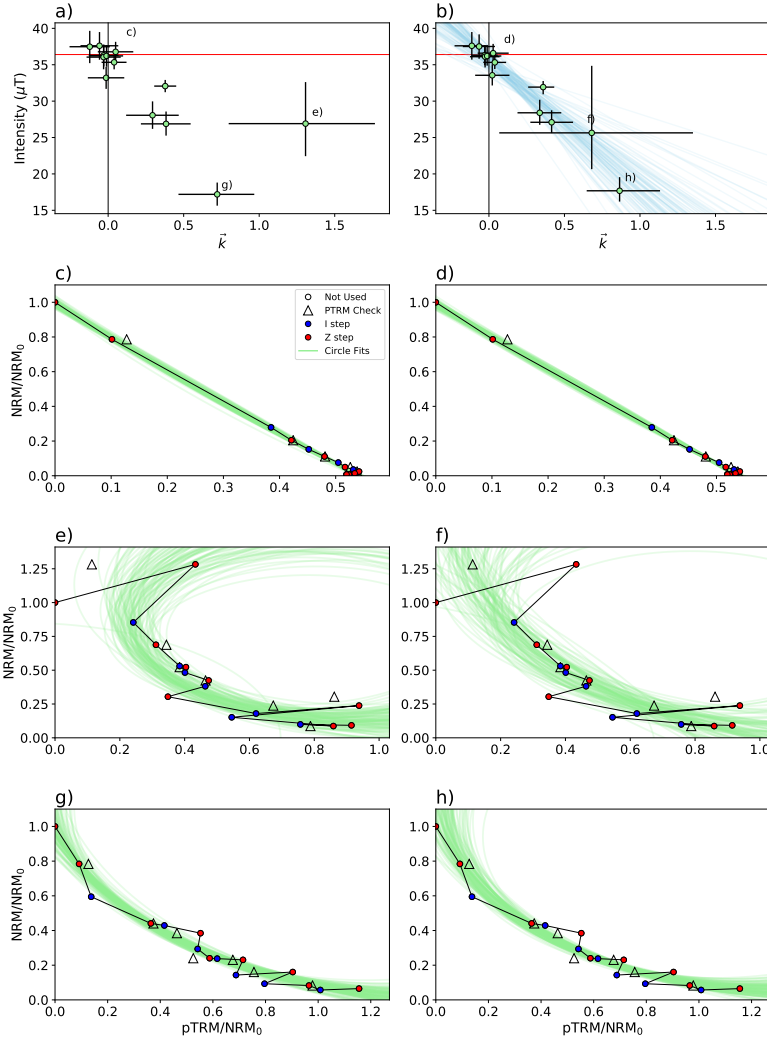


**Figure 5.** Examples demonstrating how the predicted  $\vec{k}$  and  $B_m$  for each specimen are modified for a site by using a hierarchical model (Equation 14). The left column shows draws from the posterior for an “unpooled” model where we estimate  $B_m$  and  $\vec{k}_m$  independently. The right column shows draws from the posterior for the BiCEP method where we assume a linear relationship between  $B_m$  and  $\vec{k}_m$ . a) Red horizontal line is  $B_{exp}$  (hw126, see Table 1). 95% credible intervals for  $\vec{k}_m$  and  $B_m$  are plotted using black error bars, with the medians as green points. b) Representative draws from the posterior distribution are plotted as blue lines assuming that the individual specimen values  $B_m$  follow the relationship stated in Equation 14. Note that the higher curvature specimens with large uncertainty in  $\vec{k}$  follow a linear trend away from  $B_{exp}$ . c),e),g): [Symbols same as in Figure 4.] Arai plots of particular specimens are shown with circle fits sampled from the posterior of the unpooled model shown in a) and plotted in green. In d), f), h), same specimens as in c), e), g) but using the posterior of the BiCEP model in b). Note that there is little change in the specimen in d) for which a close fit to the data is possible, but in f) and h) the curvature (and intensity) of the specimen are modified to fit the line better.

$$P(B_m|k_m, B_{anc}, \sigma_{site}, c) = \frac{1}{\sqrt{2\pi\sigma_{site}^2}} \exp\left(-\frac{(B_{anc} + c\vec{k}_m - B_m)^2}{2\sigma_{site}^2}\right). \quad (18)$$

Now we can combine our expressions for  $B_m$  and  $\vec{k}_m$  (Equations 17, Sections 2.2.1 and 2.2.2) with the new constraint of a linear relationship between  $B_m$  and  $\vec{k}_m$  (Equation 18). This allows us to obtain an expression for the site level intensity estimate  $B_{anc}$ :

$$P(B_{anc}, \sigma_{site}, c, B_m, k_m, D_m|x_m, y_m) \propto P(x_m, y_m|k_m, D_m, B_m)P(B_m|k_m, B_{anc}, \sigma_{site}, c)P(B_{anc}, \sigma_{site}, c)P(D_m, k_m). \quad (19)$$

Equation 19 may look complicated, but we defined each of the terms already. The benefit of this treatment is that we can obtain  $P(x_m, y_m|k_m, D_m, B_m)$  from our circle fitting in Equation 8 (see also Appendix 6.1). We defined  $P(B_m|k_m, B_{anc}, \sigma_{site}, c)$  in Equation 18. The values of  $\vec{k}$  and  $B_m$  for each specimen are needed to fit both of these terms. This means that specimens with large scatter in their Arai plots (those which have Arai plots that are not fit well by a line or a circle) are more strongly affected by the site level fit  $B_{anc}$ , and therefore by the specimens with more linear (or circular) Arai plots. Conversely, those specimens with a small uncertainty in  $\vec{k}$  or  $B_m$  are tightly constrained by the Arai plot fit and so have more control over the fit at the site level.

The other two terms on the right side of Equation 19 ( $P(B_{anc}, \sigma_{site}, c)P(D_m, k_m)$ ), are priors.  $P(D_m, k_m)$  were defined in Equations 14 and 16 respectively. Now, we need to define priors for  $P(B_{anc}, \sigma_{site}, c)$ . For this purpose, we use a poorly constrained prior for the slope,  $c$ , where  $P(c) \propto 1$ . Although this is not a probability distribution, the resulting posterior distribution for  $B_{anc}$  is always a real probability distribution if the number of specimens is greater than one. We use a uniform prior between 0 and 250  $\mu\text{T}$  for  $P(B_{anc})$  as intensity values can never be negative and in databases such as the MagIC database (Tauxe et al., 2016) or the PINT database of Biggin (2010) rarely (if ever) exceed 250  $\mu\text{T}$ . For  $P(\sigma_{site})$  we use a normal distribution with zero mean and standard deviation of 5  $\mu\text{T}$ , truncated to always be positive.

Figure 5b shows our median estimates for  $B_m$  and  $\vec{k}_m$  after applying the linear restriction. Here, there is a tradeoff between fitting the Arai plot data with the circle, and fitting the linear trend at a site level. The effect of the linear fitting is apparent when compared to estimating  $\vec{k}_m$  and  $B_m$  for each specimen in isolation, which is shown in Figure 5a. With the linear restriction, the  $\vec{k}$  and  $B_m$  of specimens are ‘‘pulled’’ closer to a linear trend by modifying the Arai plot fits; specimens with more uncertain  $\vec{k}_m$  are more strongly affected (e.g., specimen labeled e) and f) in Figure 5a and b). The specimens with highly linear Arai plots (for which we have small uncertainty in  $\vec{k}_m$ ), the circle fits (see g and h) are mostly unchanged. Despite this modification of the circle fits to the Arai plots by the linear model, the circle fits to those specimens do not look unreasonable.

### 2.3 Metrics of success

In order to ‘ground-truth’ the method, we rely on a compilation of paleointensity data updated from that of Paterson et al. (2014) and Tauxe et al. (2016). This compilation has data from 30 sites for which  $B_{anc}$  is well constrained (hence we use  $B_{exp}$ ), either through the IGRF, or because the specimens were given TRMs in a known lab field before the Thellier experiment. One exception to this is for hw226 and hw108, lava flows erupted in Hawaii in 1843 and 1859, prior to the range included in the IGRF. For these sites, we used the Arch3k.1 model of Korte et al. (2009). A list of sites used here is given in Table 1. Instead of choosing a range of temperatures for each site, we simply use every temperature on the Arai plot for all specimens.

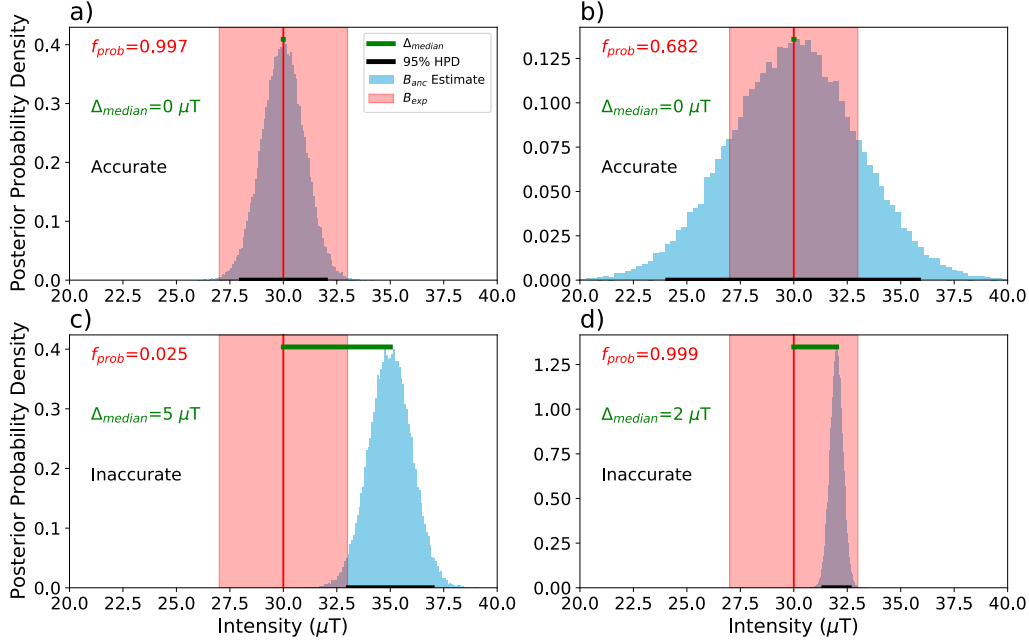


**Figure 6.** Examples of accuracy and precision metrics used in this study with simulated Gaussian distributions of  $B_{anc}$  for illustration. a) An accurate and precise estimate, b) An accurate but imprecise estimate, c) An inaccurate and imprecise estimate. d) A slightly inaccurate and highly precise estimate. Accuracy check used for  $n_{acc}$  checks whether the black line intersects the expected value ( $B_{exp}$ ).  $f_{prob}$  is the area of the blue histogram that lies within the red shaded area.  $\Delta_{median}$  is the length of the green line.

405 Because we have to estimate multiple parameters for each specimen, our method  
 406 involves a high dimensional optimization problem. Therefore, we generate the estimates  
 407 for  $B_{anc}$  for a given site using a Markov chain Monte Carlo (MCMC) method which ap-  
 408 proximates the posterior distribution by generating pseudosamples from it (see Appendix 6.2  
 409 for details). MCMC techniques are frequently used to solve high dimensional problems  
 410 of this kind.

411 For each site, we quantify the effectiveness of the BiCEP method using several met-  
 412 rics,  $f_{prob}$ ,  $\Delta_{median}$  (see Figure 6 for graphical representation),  $\bar{f}_{prob}$ , and  $n_{acc}$ :

- 413 1.  $f_{prob}$ : We report the median value of our posterior distribution and the 2.5<sup>th</sup> and  
 414 97.5<sup>th</sup> percentile of the Monte Carlo sample (95% credible interval) as error bars.  
 415 To quantify the effectiveness of our method, we look at the proportion of the pos-  
 416 terior distribution that lies within 3  $\mu$ T of the expected value of  $B$  ( $B_{exp}$ ) and call  
 417 this proportion  $f_{prob}$ .
- 418 2.  $\bar{f}_{prob}$ : the mean value of  $f_{prob}$  over all sites included in the study. A value of 1 is  
 419 the best possible value and means all our results are accurate and precise to bet-  
 420 ter than 3  $\mu$ T.
- 421 3.  $\Delta_{median}$ : the difference (in  $\mu$ T) between the median value of the MCMC sample  
 422 (see Section 6.2 for explanation) and  $B_{exp}$ . The median value of  $\Delta_{median}$  is  $\tilde{\Delta}_{median}$ .  
 423 Values of  $\tilde{\Delta}_{median}$  close to zero are best.
- 424 4.  $n_{acc}$ : the number of sites for which  $B_{exp}$  lies within our 95% credible interval. A  
 425 related parameter,  $f_{acc}$  is the fraction of results that are accurate ( $n_{acc}/n_{sites}$ ),

426 where  $n_{sites}$  is the total number of sites analyzed. We expect this number to be  
 427 0.95 in ideal circumstances.

428 We use these metrics to compare the BiCEP results to those obtained by several differ-  
 429 ent sets of selection criteria: CCRIT (Cromwell et al., 2015), Paterson’s modified PICRIT03  
 430 (here called PICRITMOD) and SELCRIT Criteria (here called SELCRITMOD, Paterson  
 431 et al., 2014). For this exercise, we also calculated these two criteria with the addition  
 432 of the curvature criterion of  $|\vec{k}| < 0.270$ , which we refer to as PICRITMODk and SEL-  
 433 CRITMODk. We apply these criteria using the standard deviation optimization method  
 434 in Thellier GUI. Most sets of commonly used selection criteria rely on an assumption of  
 435 a Gaussian probability distribution for the site level estimate  $B_{anc}$ , which allows us to  
 436 calculate these same metrics.

437 For our analyses of our success metrics, we exclude sites that contain fewer than  
 438 three specimens. For fair comparison, we do not exclude sites from our analyses with tra-  
 439 ditional selection criteria which have high standard deviation, as we do not do this for  
 440 BiCEP. If a site fails to produce an estimate of  $B_{anc}$  for any reason (for example, selec-  
 441 tion criteria passed less than two specimens), we assume the prior distribution of a uni-  
 442 form distribution between 0 and 250  $\mu T$ . This allows us to compare methods directly,  
 443 with a penalty applied for excluding sites. An excluded site will have  $f_{prob}=0.012$ , whereas  
 444 a site with a highly inaccurate result can have  $f_{prob}$  of 0, so exclusion is considered only  
 445 slightly better than an inaccurate result in this scheme. We discuss the results of this  
 446 comparison in Section 3.1.

#### 447 2.4 Width of prior and order of fit

448 Here we consider several alternative contingent models in order to explore our choices  
 449 for  $P(\sigma_{site})$  and assumptions about the relationship of  $B_m$  and  $\vec{k}$ . In addition to using  
 450 a standard deviation of 5  $\mu T$  for  $P(\sigma_{site})$ , we use standard deviations of 10  $\mu T$  and 20  
 451  $\mu T$ . The effect of this is hard to conceptualize, but wider priors will prioritize fitting cir-  
 452 cles to the individual specimens over fitting the linear relationship between  $B_m$  and  $\vec{k}_m$   
 453 at a site level. The practical effect of this is wider posteriors for sites where the num-  
 454 ber of specimens is small.

455 So far, we have assumed *a priori* that  $B_m$  is linearly dependent on  $\vec{k}_m$ . Because  
 456 there is no theoretical reason why this should be the case, we test models for which the  
 457 relationship between  $B_m$  and  $\vec{k}_m$  is described by a quadratic polynomial and a cubic poly-  
 458 nomial. We would expect a higher order model to more closely fit the individual  $\vec{k}_m$  and  
 459  $B_m$  values, but with a loss of precision due to the more complicated model.

460 Results for our method, as well as for two sets of selection criteria, are given in Ta-  
 461 ble 2. For each model, we calculate  $\bar{f}_{prob}$ ,  $\tilde{\Delta}_{median}$  and  $f_{acc}$  for comparison. In this ta-  
 462 ble, our models are named for the value of the standard deviation of  $P(\sigma_{site})$  as well as  
 463 the order of the fit. Our preferred model is referred to as “Linear 5  $\mu T$ ”, and this is the  
 464 model used in this paper where otherwise unspecified.

#### 465 2.5 MCMC sampler diagnostics

466 MCMC samplers are only ever an approximation of the posterior distribution, and  
 467 the number of Monte Carlo samples needed to make an accurate approximation is not  
 468 the same for every site, or every run of the sampler. To determine whether we are ac-  
 469 curately sampling the posterior distribution, we look at three diagnostics which are also  
 470 described in Appendix 6.2:

- 471 1.  $\hat{R}$ : (Gelman & Rubin, 1992) quantifies convergence between chains in the MCMC  
 472 method. This parameter is required to be between 1.1 and 0.9 for the sampler to  
 473 converge.
- 474 2.  $n_{eff}$ : the effective MCMC sample size. We are using 30,000 Monte Carlo samples  
 475 and  $n_{eff}$  should be large ( $> 1000$ ) to have a good representation of our param-  
 476 eters.
- 477 3.  $f_{div}$ : the proportion of divergent transitions  $f_{div}$  in the MCMC sample. This should  
 478 ideally be zero, but it does not appear to cause large problems for the estimate  
 479 of  $B_{anc}$  if it is non zero (see Section 6.2).

480 The diagnostics  $n_{eff}$  and  $\hat{R}$  are produced for each of our parameters (each of our  
 481  $B_m, \vec{k}_m, D_m$  and  $B_{anc}, \sigma_{site}$ ). When reporting these values, we look at the worst value  
 482 of  $\hat{R}$  (furthest from unity) and the value of  $n_{eff}$  for  $B_{anc}$ . If  $\hat{R} > 1.1$ , we replace the dis-  
 483 tribution on  $B_{anc}$  with a uniform distribution between 0 and 250  $\mu\text{T}$  (the prior). The  
 484 results of the MCMC sampler are presented in Section 3.4.

### 485 3 Results

#### 486 3.1 Comparison of BiCEP to Selection Criteria

487 In this section, we compare the BiCEP to several sets of selection criteria (see Sec-  
 488 tion 2.3). The full set of results for all sites can be seen in Figure 7, and are summarized  
 489 in Supplementary Data Set S1.

Model Name	$\bar{f}_{prob}$	$\hat{\Delta}_{median}$ ( $\mu\text{T}$ )	$f_{acc}$	Number of Sites
Linear, 5 $\mu\text{T}$ (BiCEP)	0.63	1.7	0.85	25
Linear, 10 $\mu\text{T}$	0.62	1.7	0.85	25
Linear, 20 $\mu\text{T}$	0.61	1.7	0.85	25
Quadratic, 5 $\mu\text{T}$	0.56	1.7	0.81	25
Quadratic, 10 $\mu\text{T}$	0.55	1.6	0.85	25
Quadratic, 20 $\mu\text{T}$	0.55	1.8	0.85	25
Cubic, 5 $\mu\text{T}$	0.45	2.6	0.85	22
Cubic, 10 $\mu\text{T}$	0.45	2.3	0.85	24
Cubic 20 $\mu\text{T}$	0.44	2.5	0.85	24
CCRIT	0.47	1.9	0.88	22
PICRIT (Modified)	0.56	2.2	0.77	23
PICRIT (Modified with $\vec{k}$ )	0.61	1.9	0.69	21
SELCRIT (Modified)	0.53	2.9	0.58	25
SELCRIT (Modified with $\vec{k}$ )	0.58	2.3	0.58	23

**Table 2.** Results comparing the models used in this study to results using CCRIT (Cromwell et al., 2015) as well as PICRITMOD and SELCRITMOD (Paterson et al., 2014), both with and without the  $\vec{k}$  criterion. See details in text and Figure 6 for explanations of the different parameters presented here. Results are sorted by the number of specimens in the site used to make the estimate using our method.

490 Figure 7 shows the 95% credible intervals for each method, normalized by the ex-  
 491 pected value at the site. The median values of our results are generally similar to those  
 492 found by our selection criteria. BiCEP yields the largest number of accurate and pre-  
 493 cise results, with CCRIT being generally less precise and slightly less accurate. PICRIT-  
 494 MOD and SELCRITMOD are generally less accurate and precise than BiCEP, however

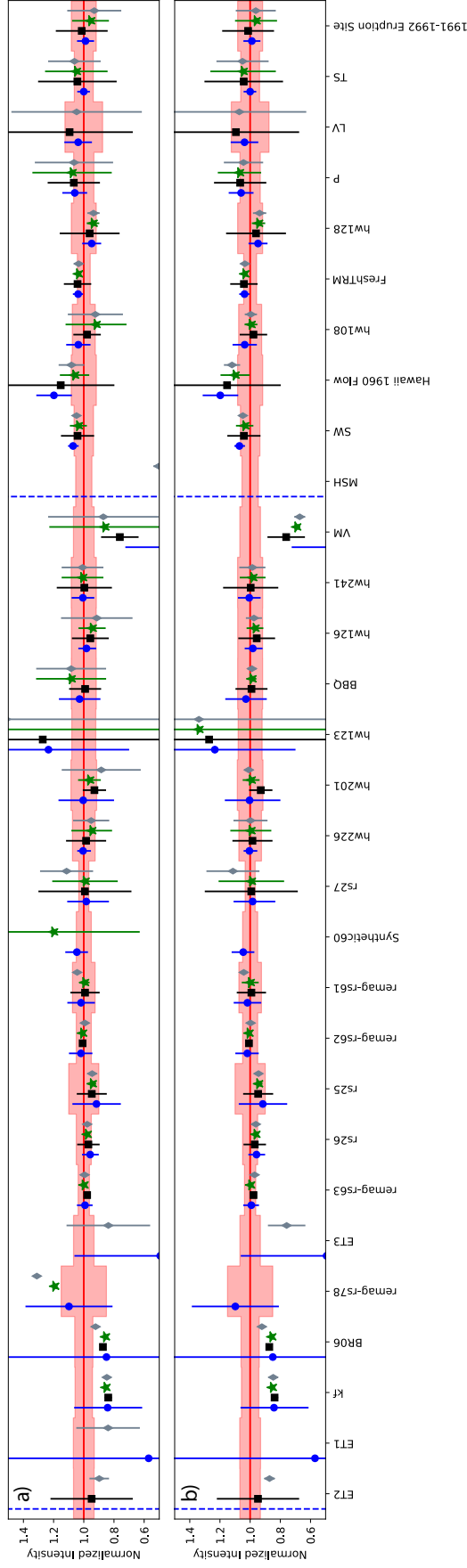


**Figure 7.** In a) for our collection of sites, we plot (Table 1) paleointensity estimates using BiCEP (blue circles) with 95% confidence interval compared to results using CCRIT (black squares), Paterson’s modified PICRITMOD (green stars) and SELCRITMOD (grey diamonds). In b), the same information is plotted, but green stars represent results from PICRITMODk and grey diamonds represent results from SELCRITMODk; the  $\bar{k} < 0.270$  criterion has been applied to PICRITMOD and SELCRITMOD. A dashed blue line indicates a site where the sampler failed with  $\hat{R} > 1.1$ , so the prior distribution (a uniform distribution between 0 and  $250 \mu\text{T}$ ) was used. The results are normalized to the expected field value for each site (black line, by definition 1) and the pink shaded region represents  $\pm 3 \mu\text{T}$ . Sites are ordered by the number of specimens used by BiCEP for paleointensity analysis in that site with the number of specimens increasing to the right. Results are summarized in Supplementary Data Set S1.

495 introducing the curvature criterion for PICRITMODk and SELCRITMODk improve the  
 496 accuracy and precision significantly. Both PICRITMODk and SELCRITMODk boast  
 497 highly precise estimates for passing sites, with similar levels of accuracy to BiCEP. How-  
 498 ever, this improved accuracy and precision is achieved by excluding more sites, which  
 499 penalizes these methods using our success metrics.

500 Sites in Figure 7 are sorted by the number of specimens used by BiCEP for the anal-  
 501 ysis. Unique to our method, sites with low numbers of specimens ( $M$ ) have wide cred-  
 502 ible intervals and sites with high  $M$  have narrow credible intervals, so the estimate of  
 503  $B_{anc}$  becomes more precise as more specimens are measured. This is because calculat-  
 504 ing the credible interval for a  $B_{anc}$  is more similar to calculating the standard error of  
 505 the mean than the site level standard deviation, which is done for our traditional selec-  
 506 tion criteria. The increasing precision on  $B_{anc}$  leads to some sites with high  $M$  having  
 507 estimates of  $B_{anc}$  which are seemingly too precise. These estimates are still generally only  
 508 a few  $\mu\text{T}$  away from the expected value, however, and we discuss potential reasons for  
 509 this in Section 4.4.

510 Our results in Table 2 indicate that BiCEP is the method that yields the largest  
 511 number of accurate and precise results, having a higher  $\bar{f}_{prob}$  and lower  $\bar{\Delta}_{median}$  than  
 512 all of our sets of selection criteria. For selection criteria which include a curvature cri-  
 513 terion, much of this improvement comes from BiCEP’s inclusion of accurate results for  
 514 two sites, remag-rs78 and Synthetic60. If we look exclusively at the sites which passed  
 515 each criterion, PICRITMODk and SELCRITMODk achieve higher levels of precision for  
 516 those sites (higher  $\bar{f}_{prob}$  than BiCEP if only passing sites considered), with PICRITMODk  
 517 achieving similar levels of accuracy to BiCEP (similar  $\bar{\Delta}_{median}$  for passing sites). This  
 518 higher level of precision is likely an outcome of using the standard deviation optimiza-  
 519 tion procedure, and is probably not reflective of the true uncertainty judging by the low  
 520  $\bar{f}_{acc}$  for both PICRITMODk and SELCRITMODk. CCRIT still achieves lower  $\bar{f}_{prob}$  and  
 521 higher  $\bar{\Delta}_{median}$  than BiCEP even if only passing sites are considered, indicating a slightly  
 522 lower accuracy and precision overall. Our two selection criteria which do not include a  
 523 curvature criterion (PICRITMOD and SELCRITMOD) have a larger number of pass-  
 524 ing sites, including remag-rs78 and Synthetic60, but still have reduced  $\bar{f}_{prob}$  and  $\bar{\Delta}_{median}$ .  
 525 Ultimately it seems that BiCEP offers the best of both worlds, passing at least as many  
 526 sites as the more permissive criteria, and achieving higher accuracy and more realistic  
 527 precision than the more restrictive criteria.

### 528 3.2 Width of the prior

529 To investigate the role of the prior distribution ( $P(\sigma_{site})$ ), we apply the BiCEP method  
 530 on the data compilation using a variety of values for its standard deviation (see Table 2).  
 531 The main effect of varying  $\sigma_{site}$  is that for smaller values, the estimates of  $B_m$  and  $\vec{k}_m$   
 532 for specimens are “pulled” closer to the line being fitted at a site level (see Figure 5a,b).  
 533 For our estimate of  $B_{anc}$ , this means that sites with fewer specimens will be more pre-  
 534 cise, as it is unlikely that specimen  $B_m$  will deviate strongly from the mean. For sites  
 535 with many specimens, there is little effect as  $\sigma_{site}$  is well constrained by the data.

536 From Table 2, we see that changes to  $P(\sigma_{site})$  seem to have little influence on the  
 537 effectiveness of the model, as all our  $\bar{f}_{acc}$  values are the same for our linear model regard-  
 538 less of the prior distribution used. We can also see graphically in Figure 7 that our pre-  
 539 cision is low for sites with small number of specimens ( $M$ ). Because of this, we favor the  
 540 version of the model with a 5  $\mu\text{T}$  standard deviation on  $P(\sigma_{site})$ , as models with higher  
 541 standard deviations reduce precision without capturing any more sites within their 95%  
 542 credible intervals.

543

### 3.3 Order of polynomial fit

544

545

546

547

548

549

550

551

552

553

The results for our test sites (Table 2) demonstrate that increasing the order of the polynomial fit decreases the precision of the estimate as demonstrated by reduced values of  $\bar{f}_{prob}$ . This is expected as there are more parameters to be estimated with the same number of data. The level of accuracy is not significantly improved by increasing the model order. The best quadratic model produced a  $\hat{\Delta}_{median}$  of  $1.6 \mu\text{T}$ , which is not a significant improvement over the value of  $1.7 \mu\text{T}$  for the best linear model to account for the reduction in precision. The number of passing sites is reduced for the cubic model, indicating that the sampler is struggling to fit this model. Consequently, the cubic model produces more inaccurate and less precise results. For this reason, we assume a linear relationship between  $B_m$  and  $\vec{k}_m$ .

554

### 3.4 Sampler Diagnostics

Site Name	Worst $\hat{R}$	$n_{eff}$	$f_{div}$
1991-1992 Eruption Site	1.00	59741	0.00
hw108	1.00	77959	0.00
hw123	1.01	11687	0.00
hw126	1.00	36130	0.01
hw128	1.00	78978	0.00
hw201	1.00	10641	0.01
hw226	1.00	7139	0.05
hw241	1.00	66565	0.00
BR06	1.01	451	0.00
P	1.00	62252	0.00
VM	1.05	1447	0.00
BBQ	1.00	63082	0.00
rs25	1.00	5614	0.00
rs26	1.00	11866	0.00
rs27	1.00	22211	0.00
remag-rs61	1.00	26746	0.00
remag-rs62	1.00	16916	0.00
remag-rs63	1.00	3788	0.00
remag-rs78	1.00	12388	0.00
kf	1.02	2712	0.00
Hawaii 1960 Flow	1.00	60184	0.00
SW	1.00	36390	0.00
TS	1.00	56518	0.00
ET1	1.01	995	0.00
ET2	6.93	6	0.03
ET3	1.01	424	0.00
Synthetic60	1.00	36572	0.01
LV	1.02	5931	0.08
MSH	2.78	24	0.45
FreshTRM	1.00	81007	0.00

**Table 3.** Sampler diagnostics (see Section 2.5 for an explanation of each diagnostic) for each site using the BiCEP method.

555

556

The sampler diagnostics for each site are given in Table 3. Indicators of poor MCMC sampler performance (worst  $\hat{R} > 1.1$ , low  $n_{eff}$ , high  $f_{div}$ ) tend to occur at sites with four

557 or fewer specimens, or for specimens where the Arai plots are extremely scattered and  
 558 the sampler struggles to fit them. In the latter case, it may be possible to exclude these  
 559 specimens by looking at which specimen level parameters have high  $\hat{R}$ , as this indicates  
 560 that fitting a circle to these specimens is inappropriate. We did not exclude specimens  
 561 on this basis in our analysis, however, we include an option to do this in the BiCEP GUI  
 562 software (see Appendix 6.3).

563 The prevalence of high  $\hat{R}$  for sites with low numbers of specimens indicates that  
 564 to get a strongly reproducible answer from this method, paleomagnetists ought to mea-  
 565 sure five or more specimens per site. In practice, most studies already do this in order  
 566 to have enough specimens that pass the chosen selection criteria, yet many specimens  
 567 may be excluded from analysis. Here, we can use all of the specimens measured so there  
 568 may be no additional burden.

### 569 3.5 Summary of Results

570 After testing all of our contingent models, we prefer the model which assumes the  
 571 relationship between  $B_m$  and  $\vec{k}_m$  is linear, and which uses a  $5 \mu\text{T}$  standard deviation on  
 572  $P(\sigma_{site})$ . This model performs better than classical sets of selection criteria, either pass-  
 573 ing a greater number of sites (than CCRIT, PICRITMODk, SELCRITMODk) or hav-  
 574 ing significantly higher accuracy and precision (than PICRIT, SELCRIT). Our preci-  
 575 sion increases for sites for which the number of specimens is large, similar to calculat-  
 576 ing the standard error of the mean when using selection criteria. Unlike selection crite-  
 577 ria, the BiCEP method does not require exclusion of large numbers of specimens to ob-  
 578 tain an accurate result, which leads us to prefer it over those methods.

## 579 4 Discussion

### 580 4.1 Advantages of BiCEP compared to selection criteria

581 BiCEP has significant advantages over the classical selection criteria approach. Firstly,  
 582 we obtain paleointensity estimates for all sites with at least three specimens, including  
 583 some which do not contain any specimens that would pass classical selection criteria (see  
 584 Figure 7). In most cases, our estimates have similar or higher accuracy than the selec-  
 585 tion criteria approach (evidenced by  $\hat{\Delta}_{median}$  and Figure 7), and this is accomplished  
 586 while only excluding specimens from the analysis which were not fully demagnetized. In  
 587 some cases, our method yields results even if none of the selection criteria accept any spec-  
 588 imens or are inaccurate. For example, for sites remag-rs78 and Synthetic60, our strict  
 589 criteria (CCRIT, PICRITMODk, SELCRITMODk) produce no results, and our more  
 590 permissive criteria (PICRITMOD, SELCRIT) produce less accurate (and in the case of  
 591 Synthetic60, much less precise) results than BiCEP.

592 Secondly, the increasing precision of our paleointensity estimate as the number of  
 593 specimens increases allows for an improved workflow when compared to classical paleo-  
 594 intensity criteria. Instead of needing a minimum number of specimens to pass our se-  
 595 lection criteria, we can keep measuring specimens until we reach a desired level of pre-  
 596 cision. We discuss this workflow in more detail in Section 4.3. The property of increas-  
 597 ing precision with number of specimens is inherent to Bayesian models and can also be  
 598 found in the method of Kosareva et al. (2020), although their method does not include  
 599 the bias correction found in our method.

600 Thirdly, the BiCEP method propagates the uncertainties from a specimen to the  
 601 site level. Specimens with more scattered (or non linear, or non circular) Arai plots will  
 602 have less influence over the specimen mean than those with highly linear Arai plots. In  
 603 addition to this, the BiCEP method foregoes the need for criteria which are concerned  
 604 with the length of the line on the Arai plot used to make an interpretation, like the NRM

605 Fraction (e.g., FRAC of Shaar & Tauxe, 2013). Using a set of temperatures with small  
 606 FRAC will cause an increase in the uncertainty in  $\vec{k}$  (see Figure 4e, f), which will cause  
 607 this specimen to have less effect on the estimate of  $B_{anc}$ , without excluding it from the  
 608 analysis entirely. We discuss this further in Section 4.5.

609 **4.2 Predictive ability of the method**

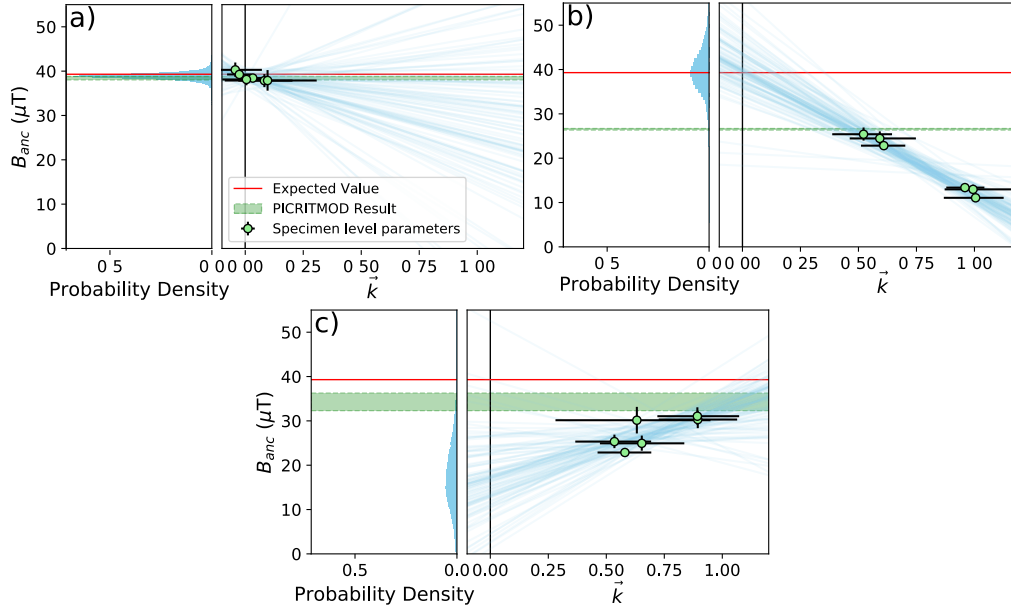


**Figure 8.** Example of the BiCEP method applied to three subsets of 6 specimens from site hw108 ( $B_{exp} = 39.3 \mu T$ ). The left column in each subplot shows histograms of the BiCEP results, and the right column shows plots of specimen  $\vec{k}$  vs  $B_{anc}$  with the BiCEP line fits. Light green shaded regions with dashed edges represent the  $2\sigma$  interval of the PICRITMOD estimate for these subsamples. In a) there is a small range of  $\vec{k}$  and  $B_{anc}$  values which leads to an imprecise estimate of  $c$ , but an accurate and precise estimate of  $B_{anc}$ . In b) there is a large range of values on  $\vec{k}$ , but all specimens have high  $\vec{k}$ . This leads to an estimate with a relatively precise estimate of  $c$ , and an accurate but imprecise estimate of  $B_{anc}$ . In c) there is a reasonably small range of values on  $B_{anc}$ , and the relationship between  $B_{anc}$  and  $\vec{k}$  is not linear, but BiCEP attempts to find a linear model. This leads to an imprecise and inaccurate estimate of both  $c$  and  $B_{anc}$ .

610 Although our results are promising, it is worth noting that traditional selection cri-  
 611 teria also perform well for the majority of our sites. To see if the BiCEP method offers  
 612 accurate results with poorer quality data, we subsampled results from site hw108, which  
 613 had a range of good and poor quality specimens. Figure 8 shows the results of BiCEP  
 614 applied to three different subsets of six specimens taken from this site, along with the  
 615 results of the PICRITMOD criteria applied to this site (in green). It is worth noting that  
 616 only the specimens in Figure 8a would pass the CCRIT criteria which gave a highly ac-  
 617 curate result (within 1  $\mu T$ ), or any of our more restrictive criteria.

618 We identify three behaviours for which BiCEP results deviate from a linear model  
 619 with high precision on the slope and intercept. Figure 8a shows a subset of specimens  
 620 for which the range of  $\vec{k}$  values of the specimens is very small, and so the uncertainty

621 of the slope of the linear relationship between  $\vec{k}_m$  and  $B_m$  ( $c$ ) is high. In this case, how-  
 622 ever, because these specimens all have  $\vec{k}$  close to zero, the estimate of  $B_{anc}$  is accurate  
 623 and precise. Figure 8b shows a different subset of specimens for which the range of  $\vec{k}$  val-  
 624 ues is large, but there are no  $\vec{k}$  values close to zero. This results in an estimate of  $B_{anc}$   
 625 which is still accurate, but imprecise due to the uncertainty in extrapolating the linear  
 626 relationship between  $\vec{k}_m$  and  $B_m$  back to zero. The PICRITMOD result for this subset  
 627 returns an average value which underestimates  $B_{exp}$  by around  $\sim 13 \mu\text{T}$  or  $\sim 30\%$ , and  
 628 criteria using the curvature criterion return no values, as all specimens have curvature  
 629 values higher than the threshold. The high uncertainty in  $B_{anc}$  might still be considered  
 630 a problem, but this result indicates that measuring more specimens would likely yield  
 631 a more precise result.

632 Figure 8c shows a set of specimens where the range of  $\vec{k}$  is low, so the  $\vec{k}_m$  versus  
 633  $B_m$  relationship is not particularly linear. BiCEP attempts to find a linear trend with  
 634 these data, and extrapolates back to a  $B_{anc}$  which is both highly inaccurate and impre-  
 635 cise. This might be considered a problem for BiCEP, but it is possible to detect such be-  
 636 havior as the uncertainty on both  $B_{anc}$  and the slope relating the  $B_m$  versus  $\vec{k}_m$  ( $c$ ) are  
 637 large. This indicates to us that we can use a metric of the uncertainty in both the slope  
 638 and intercept of the linear fit in BiCEP to decide whether a site level result is accurate  
 639 or not. This leads us to a laboratory workflow which uses BiCEP results to decide if a  
 640 site is acceptable, might be acceptable with further work or is unlikely to give a reason-  
 641 able result.

### 642 4.3 Workflow with BiCEP

643 Figure 9 plots the 95% credible interval on  $B_{anc}$  as a percentage against the 95%  
 644 credible interval on  $c$  as a proportion of the median  $\tilde{B}_{anc}$  for all sites where  $\hat{R} > 1.1$ .  
 645 The sizes of the points on the plot represents the number of specimens per site ( $M$ ), with  
 646 squares representing sites with  $M < 5$ . The colors show the percentage deviation from  
 647  $B_{exp}$  using BiCEP, with redder colors for more inaccurate results. With the exception  
 648 of two sites (VM and hw123), as the number of specimens increases, sites trend towards  
 649 the bottom left region of this plot, indicating an increase in precision. This has dimin-  
 650 ishing returns as the number of specimens increases above five. The increase in preci-  
 651 sion is also accompanied with an increase in accuracy. Almost all sites with an estimated  
 652 precision on  $B_{anc}$  better than 40% have median values within 20% of  $B_{exp}$ . Our outlier  
 653 sites VM and hw123, which are imprecise despite having large numbers of specimens ( $M=12$   
 654 and 18 respectively), are also inaccurate. This indicates that the width of the 95% cred-  
 655 ible intervals is a useful statistic for diagnosing inaccuracy in the BiCEP method.

656 We have divided Figure 9 into four regions (labeled A-D). Sites in region A have  
 657 high precision on both  $B_{anc}$  and  $c$  and are representative of the results for the major-  
 658 ity of sites in this study; sites in this region are highly accurate. Sites in region B have  
 659 high precision on  $B_{anc}$  (better than 40%, which for a Gaussian distribution would be equiv-  
 660 alent to a standard deviation of  $\pm 10\%$ ) but low precision on  $c$  (95% credible interval on  
 661  $c/\tilde{B}_{anc} > 1$ ). These sites are usually analogous to the example shown in Figure 8a, with  
 662 low Arai plot curvature and similar intensities for all specimens. Sites in region C have  
 663 high precision on  $B_{anc}$  but a low precision on  $c$ . These sites may have a large number  
 664 of curved specimens which follow a linear trend that can be extrapolated back to the cor-  
 665 rect  $B_{exp}$ , and are analogous to our example in Figure 8b. Region D is representative  
 666 of the worst constrained estimates, with low precision on  $B_{anc}$  and  $c$ . Sites in this re-  
 667 gion may have highly inaccurate estimates of  $B_{anc}$ , often with low  $M$ . If these sites have  
 668 high  $M$ , they may be similar to our example in Figure 8c in which a linear relationship  
 669 between  $B_{anc}$  and  $c$  is not well determined, and the average  $|\vec{k}|$  is large, leading to an  
 670 inaccurate estimate of  $B_{anc}$ .

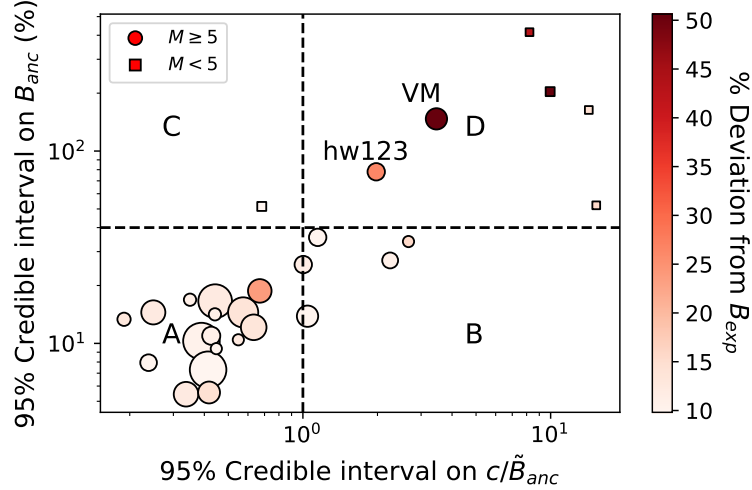


**Figure 9.** Plot of the 95% credible interval on  $B_{anc}$  against the 95% confidence interval on  $c$  (slope between intensity estimate and  $\vec{k}$ ), normalized by the median  $B_{anc}$  for all sites with  $\hat{R} < 1.1$ . Circles indicate sites for which the number of specimens  $M \geq 5$ , and squares indicate sites where  $M < 5$ . Colors indicate the deviation of the median value of the estimate from the expected site value ( $B_{exp}$ ) as a percentage. The size of markers is used to represent  $M$ . The horizontal dashed line indicates a value of 40% for the full width of the 95% credible interval on  $B_{anc}$ , which for a Gaussian distribution would correspond to a standard deviation of  $\pm 10\%$ . The vertical dashed line represents a value of 1 for the 95% confidence interval of  $c/\vec{B}_{anc}$ . Suggested workflow for sites in regions: A) or B), accept the site or continue measuring if improve precision is desired. C) Continue measuring specimens, as improved precision is likely. D) If  $M \geq 5$  stop measuring the site as further effort is likely to be futile. Otherwise continue measuring specimens until  $M = 5$ .

671 Considering the region in which a particular site plots leads to a workflow based  
 672 on the likelihood of success. In general, sites with very low numbers of specimens, ( $M =$   
 673  $2$  or  $3$ ), will begin in region D, and migrate to regions C, B or A as  $M$  increases to around  
 674 five. If a site has migrated to region A or B after five specimens have been measured,  
 675 then we likely have an accurate and precise estimate of  $B_{anc}$ , and we can finish measur-  
 676 ing specimens (or continue to measure if a higher level of precision is desired). If a site  
 677 has migrated to region C, it is likely that our estimate is accurate and that our uncer-  
 678 tainty in  $B_{anc}$  can be reduced by increasing the number of specimens. If our site remains  
 679 in region D after five specimens have been measured, the site level estimate may be in-  
 680 accurate, and measuring more specimens would be unlikely to reduce the site level un-  
 681 certainty.

682 Because the regions in Figure 9 define a workflow based on measuring five spec-  
 683 imens, we wanted to test whether our methodology could identify sites which will remain  
 684 in region D after a large number of specimens were measured. We randomly subsampled  
 685 100 sets of 5 specimens from sites hw108, VM and hw123 and calculated  $B_{anc}$  and  $c$  us-  
 686 ing BiCEP. Site hw108 was chosen because contains specimens which exhibit a wide range  
 687 of behaviours, with a large number of specimens having high  $\vec{k}$ , but yields an accurate  
 688 result. Sites VM and hw123 were chosen because these are our sites which remain in re-  
 689 gion D after measuring a large number of specimens. Our results for these three sites  
 690 are given in Supplemental Figure S2. Our subsampled hw108 obtained results in region

691 D 5 times out of 100, whereas our subsampled VM and hw123 obtained results in region  
 692 D 94 and 90 times respectively. This indicates that sites which remain in region D af-  
 693 ter measuring 5 specimens are likely to remain there after measuring many more, and  
 694 so measuring more specimens is usually a futile effort.

#### 695 **4.4 Overly precise estimates of $B_{anc}$**

696 The BiCEP method has a lower  $f_{acc}$  than CCRIT, despite having a similar degree  
 697 of accuracy when using a metric like  $\Delta_{median}$ . The reason for this is that the increas-  
 698 ing precision on the BiCEP estimate leads to estimates which are highly precise when  
 699  $M$  is large. This is the case shown in Figure 6d.

700 Labeling sites with extremely high precision in the estimate as inaccurate may be  
 701 misleading, as we have not taken into account uncertainties in the value of the expected  
 702 fields at the sites in this study. For example, using differences between the observed di-  
 703 rections and the IGRF, Yamamoto and Hoshi (2008) quoted the expected value at the  
 704 site “SW” as  $46.0 \pm 2.6 \mu\text{T}$ , which is just consistent with the 95% credible interval for our  
 705 specimen (48.2-49.7  $\mu\text{T}$ ). Because of this, we prefer to use  $\bar{f}_{prob}$  as a metric of how well  
 706 a model performs as it allows for a few  $\mu\text{T}$  of uncertainty in the expected field value. Ad-  
 707 ditionally, Yamamoto and Yamaoka (2018) suggested that the IZZI-Thellier results for  
 708 sites SW and TS may be biased slightly high due to acquisition of a thermo-chemical re-  
 709 manent magnetization (TCRM), which is not detectable by our method. Yamamoto et  
 710 al. (2003) also invoke a TCRM mechanism to explain the paleointensity overestimate for  
 711 the Hawaii 1960 Flow, which is another of their sites for which we overestimate the ex-  
 712 pected intensity (see Figure 7 and Supplementary Data Set S1). We note that Cromwell  
 713 et al. (2015) also sampled the 1960 flow (hw241 which targeted the fine grained flow top)  
 714 and all selection criteria resulted in accurate results, with BiCEP producing the tight-  
 715 est confidence interval.

#### 716 **4.5 Exclusion of measurement level data**

717 It is frequently possible to improve the accuracy and precision of results by find-  
 718 ing the ‘best’ set of temperature steps to use in the intensity interpretation. Two situ-  
 719 ations frequently occur for which this might be justified. The first is the case in which  
 720 thermochemical alteration occurs at high temperature (e.g., Figure 4e). For such spec-  
 721 imens, the low temperature measurements can be used to make a paleointensity estimate  
 722 (colored dots in the figure). Figures 4e and f show how our method can be used on a re-  
 723 duced range of temperature steps on the Arai plot at the cost of precision. The plot of  
 724 circle fits (green lines in Figure 4e) demonstrates that the Arai plot interpretations are  
 725 poorly constrained and can continue in any direction after the last temperature step cho-  
 726 sen. This results in a higher uncertainty in the curvature associated with this (Figure 4f).  
 727 The second case in which a portion of the data could be excluded from the calculation,  
 728 would be when the magnetization has multiple components (Figure 10a). In such a case,  
 729 a paleointensity estimate can only be made using the small range of temperature steps  
 730 that correspond to the characteristic component. We currently do not have an objec-  
 731 tive method to choose which set of temperature steps on the Arai plot to use. We sug-  
 732 gest that decisions about which data points to include should not be made based on the  
 733 original in-field or zero field Arai plot measurements (dots in the Arai plots), but rather  
 734 exclusively on deviating pTRM checks (triangles in, e.g., Figure 4e) or other indicators  
 735 of alteration for the first case and on the directions of the magnetization vector (it must  
 736 trend to the origin and be well defined) in the second case, e.g., Figure 10a.

737 Caution should be used when excluding a particular temperature steps for reasons  
 738 other than this. If the set of temperature steps chosen does not represent the charac-  
 739 teristic component of magnetization, this can alter the outcome of the BiCEP method, es-  
 740 pecially if a large part of the Arai plot is excluded. Additionally, excluding more points

741 on the Arai plot tends to increase the chance that a specimen will cause  $\hat{R}$  failure. As  
 742 such, we recommend using as many points on the Arai plot as possible unless done for  
 743 one of the reasons stated above.

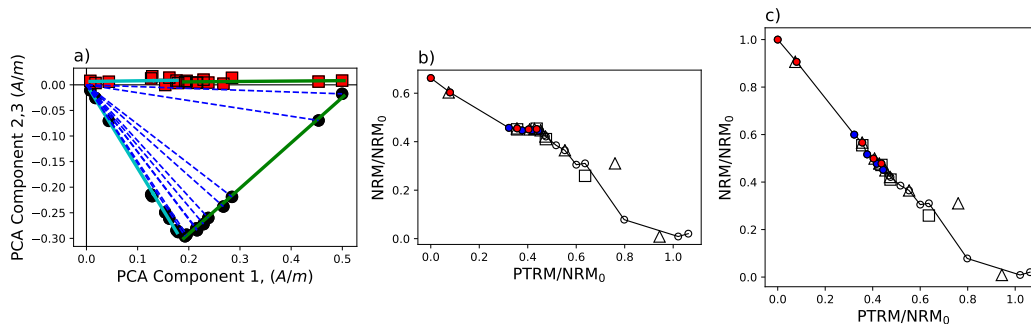


**Figure 10.** a) Example of vector endpoint diagram for specimen FB2-B1 from Lisé-Pronovost et al. (2020). The magnetization is rotated so that the principal component of the TRM direction for all steps lies along the x axis. Green line fit to the low temperature component and cyan line fit to the high temperature component. b) Arai plot and c) “corrected” Arai plot for a specimen from the data shown in b). NRM values for the low temperature component (filled circles) are usually calculated by taking the magnitude of the vector endpoint (blue dashed lines in the vector endpoint diagram in a). In c), these NRM values are calculated by vector subtracting the high temperature component (cyan line), taking the magnitude of our new NRM vectors (distance along green line), and adding the magnitude of the low temperature component (length of cyan line). Both b) and c) are scaled by the total NRM distance along both components (total distance along both green and cyan lines).

#### 744 4.6 Application to multi-component magnetizations

745 We test an application of the BiCEP method on data with multi-component di-  
 746 rections as shown in Figure 10a using the data of Lisé-Pronovost et al. (2020). The data  
 747 are from Scottish firebricks which were used in a foundry in Australia. The date and lo-  
 748 cation of firing are both well constrained, hence we have a reasonably well constrained  
 749 value for  $B_{exp}$ . The bricks all contained a low temperature component associated with  
 750 the Australian field. Some also displayed a high temperature component associated with  
 751 the original firing in Scotland as shown in Figure 10a. Lisé-Pronovost et al. (2020) al-  
 752 ready have interpretations which separate these components in the original study. To  
 753 account for the change in direction of the NRM, we subtract the high temperature  
 754 component from the low temperature component, and then add the magnitude of these val-  
 755 ues to the magnitude of the low temperature component (see Figure 10 for a graphical  
 756 explanation). The vector subtraction is necessary for the low-temperature component  
 757 as we need a total TRM ( $pTRM_{max}$ ) to scale by in order to penalize the result for shorter  
 758 components. We then proceed to use the BiCEP method as previously described, using  
 759 the original interpretations for the different components. For the sake of simplicity, we  
 760 do not perform the magnetomineralogical change (MMC) correction (Valet et al., 1996).  
 761 We also do not apply the corrections for anisotropy of TRM or cooling rate with these  
 762 data, as they appeared to be negligible. Of course these could be applied in the usual  
 763 fashion if necessary.

764 We display the results from multi-component remanences in Figure 11. We find that  
 765 for the low temperature, Australian field, component (Figure 11a), our estimates for all  
 766 firebricks contain the expected answer ( $61.17 \mu T$ ) within the 95% credible interval. Our

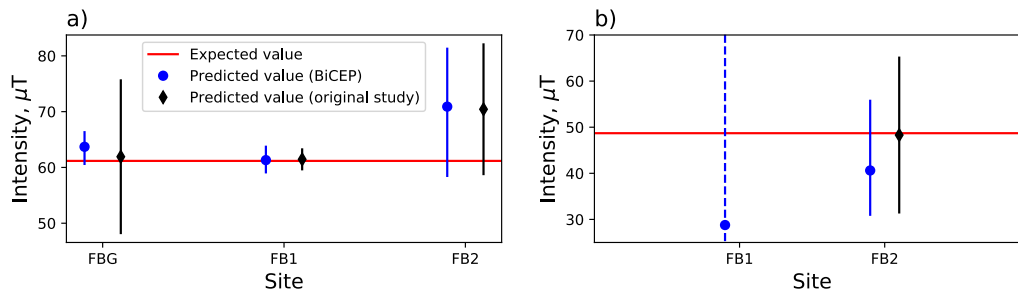


**Figure 11.** Expected and predicted intensities on the data of Lisé-Pronovost et al. (2020) using BiCEP (blue circles) and the method used in the original study (black diamonds). a) Results for the low temperature component (Australia, expected field value  $61.17 \mu\text{T}$ ) for each firebrick. b) Results for the high temperature component (Scotland, expected field value  $48.3 \mu\text{T}$ ), where this component was present. The dashed blue line indicates that the MCMC sampler failed to converge for site FB1.

767 interpretation for site FBG is slightly less accurate than the original analysis but with  
 768 much higher precision. This difference is likely caused by not applying the MMC cor-  
 769 rection, as the specimens at this site were mostly of good quality, with none being ex-  
 770 cluded from the original analysis.

771 For the high temperature component (Figure 11b) our results behave differently.  
 772 The sampler does not converge for site FB1, indicating too few specimens in the anal-  
 773 ysis. For site FB2, we have a result that is less accurate, but more precise than in the  
 774 original study. The lack of MMC correction may contribute to the decreased accuracy  
 775 in this example, whereas the reduced precision is likely caused by the smaller length of  
 776 the interpretation on the Arai plot, leading to a higher uncertainty in the curvature for  
 777 that specimen. Our results for this study demonstrate that BiCEP will obtain precise  
 778 estimates for components which represent most of the magnetization, and be imprecise  
 779 for components which have small NRM fraction.

#### 780 4.7 Implications for bias in curved Arai plots

781 The success of our method demonstrates that Arai plot “curvature” or sagging does  
 782 lead to a progressive bias in paleointensity estimation which increases as the amount of  
 783 curvature increases as described by Tauxe et al. (2021) and strongly suggested by the  
 784 data of Krása et al. (2003) (see Figure 1). Our estimates are made by using the tangent  
 785 to a circle fit rather than fitting a line to part of the data, so one might expect them to  
 786 be biased. However, it has been demonstrated by e.g. the data of (Krása et al., 2003)  
 787 that fitting lines to the high temperature or low temperature slope of Arai plots yields  
 788 even more biased results than using the total TRM, which is more similar to the tan-  
 789 gent. The scaling used by our method incorporates the added uncertainty in the line slope  
 790 and  $k$  associated with choosing one of these slopes, which allows for more consistent anal-  
 791 ysis between specimens with interpretations of varying quality. The bias seen generally  
 792 underestimates paleointensity with higher (positive) curvature, but this is not the case  
 793 for all sites, some of which exhibit the opposite trend.

794 The assumption of a quasi-linear dependence between the specimen level paleoin-  
 795 tensities and the curvature of the Arai plot does not have any theoretical basis. This does  
 796 imply that the curvature is linearly related to the change in TRM susceptibility (or de-  
 797 cay of the original magnetization) between the original and lab coolings, a relationship

798 which should be further investigated. We stress that this relationship only needs to be  
 799 loosely followed for our method to work. In cases where there does not appear to be a  
 800 strong linear relationship between  $B_m$  and  $\vec{k}_m$  (e.g. in Figure 8a), an accurate paleoin-  
 801 tensity estimate is still possible if there are enough specimens with low  $|\vec{k}|$ , as the inter-  
 802 cept of the linear fit is still well constrained even if the slope is not. Conversely, if there  
 803 are few specimens with low  $|\vec{k}|$  and there is a poor linear relationship, then both the slope  
 804 and intercept are poorly constrained, resulting in a huge uncertainty in  $B_{anc}$ , as is seen  
 805 in Figure 8c.

## 806 5 Conclusions

- 807 • We present a new Bayesian method (BiCEP) which accounts for bias in paleoin-  
 808 tensity estimates in specimens.
- 809 • Instead of excluding specimens from the paleointensity analysis in the traditional  
 810 (binary) selection criteria based approach, our method predicts an amount of bias  
 811 for each specimen, using the curvature of the Arai plot as a metric of non-linearity  
 812 and a predictor of bias. In this way, the BiCEP method is quite different from the  
 813 recently published Bayesian approach of Kosareva et al. (2020).
- 814 • When tested on a compilation of sites for which an approximate paleointensity is  
 815 known *a priori*, our method yields levels of accuracy and precision similar to, or  
 816 better than restrictive paleointensity criteria, whilst accepting as many results as  
 817 permissive criteria.
- 818 • Our method generates some slightly inaccurate paleointensity estimates with high  
 819 levels of precision, but these can generally be explained with inaccuracies in the  
 820 expected field (see Section 4.4).
- 821 • The BiCEP method handles uncertainties in a different way than using classical  
 822 selection criteria, as the uncertainty in site level estimates decreases as the num-  
 823 ber of specimens increases, but this uncertainty remains high when the number  
 824 of specimens is low due to inclusion of prior information. The Bayesian uncertain-  
 825 ties are in this way more similar to the ‘extended error bars’ in the Thellier\_GUI  
 826 auto-interpreter of Shaar and Tauxe (2013).
- 827 • We propose a workflow in which sites are accepted and measurement of specimens  
 828 can cease once a desired level of confidence in the site level estimate has been reached.  
 829 Sites which do not reach this level of confidence after measuring several ( $> 5$ ) spec-  
 830 imens likely do not contain useful information and can be discarded.

## 831 Data Availability Statement

832 Data used in this paper may be found in the MagIC database at: [https://earthref](https://earthref.org/MagIC/17104/0326fdaa-4bcf-44f3-989d-0116b9a2fb75)  
 833 [.org/MagIC/17104/0326fdaa-4bcf-44f3-989d-0116b9a2fb75](https://earthref.org/MagIC/17104/0326fdaa-4bcf-44f3-989d-0116b9a2fb75) for review and will be  
 834 available to the public at <https://earthref.org/MagIC/17104> on publication.

## 835 6 Appendix

### 836 6.1 Change of variables

837 In Section 2.2.1 we mention that we need to use a change of variables to get from  
 838 our original circle fitting parameters  $R, x_c, y_c$  to our new set of parameters  $\vec{k}, D, \phi$ . We  
 839 can use the Jacobian of the parameter change to get the new formula for the posterior  
 840 probability under our new parameters:

$$P(D, \phi, \vec{k}|x, y) = P(x_c, y_c, R|x, y) \left| \frac{\partial(x_c, y_c, R)}{\partial(D, \phi, \vec{k})} \right|. \quad (20)$$

841 We can evaluate this Jacobian as:

$$\left| \frac{\partial(x_c, y_c, R)}{\partial(D, \phi, \vec{k})} \right| = \left| \frac{\vec{k}}{|\vec{k}|^3} \left( D + \frac{1}{\vec{k}} \right) (\cos \phi + \sin \phi) \right|. \quad (21)$$

842 So our posterior looks like:

$$P(D, \phi, \vec{k} | x, y) \propto \left( \sum_{n=1}^N \sqrt{\left( \left( D + \frac{1}{\vec{k}} \cos \theta \right) - x_n \right)^2 + \left( \left( D + \frac{1}{\vec{k}} \sin \theta \right) - y_n \right)^2 - \frac{1}{|\vec{k}|}} \right)^{-N/2}$$

$$\left| \frac{\vec{k}}{|\vec{k}|^3} \left( D + \frac{1}{\vec{k}} \right) (\cos \phi + \sin \phi) \right| P(\vec{k}, \phi, D). \quad (22)$$

## 844 6.2 Markov chain Monte Carlo sampling

845 The Markov chain Monte Carlo (MCMC) sampling method generates a set of sam-  
 846 ples from the posterior probability distribution of  $B_{anc}$  which allows us to approximate  
 847 it. We use the python bindings for the Stan software package (<http://mc-stan.org>) to  
 848 generate these samples which provides diagnostic information and runs relatively quickly.  
 849 For each site we run four Markov chains and generate 30,000 samples of  $B_{anc}$  in each  
 850 chain. We discard the first half of the chain as ‘burn in’ for a total of 60,000 samples.

851 Stan provides several diagnostics that tell us whether we have successfully sampled  
 852 the posterior distribution. These include the  $\hat{R}$  score (Gelman & Rubin, 1992) which tells  
 853 us about the convergence between chains, and is required to be between 1.1 and 0.9 which  
 854 is necessary for convergence, the effective sample size,  $n_{eff}$  which should be large ( $> 1000$ )  
 855 for a good sample and the number of divergent transitions ( $f_{div}$ ) which should be zero  
 856 in ideal cases. In most cases our results display high degrees of convergence with  $\hat{R}$  close  
 857 to 1 and high effective sample sizes. Some sites included divergent transitions in small  
 858 numbers. These seem to occur at a specimen level for specimens where the posterior dis-  
 859 tribution of one of the circle parameters is long-tailed. In theory this can mean the pos-  
 860 terior was inefficiently sampled, but because these specimens generally have large un-  
 861 certainties on their  $\vec{k}$  parameter, the final results do not change, even under a change of  
 862 parameters. The sampler struggled to converge, with  $\hat{R} > 1.1$  for several sites with very  
 863 few specimens, where once again the distributions are extremely long tailed. The sam-  
 864 pler also did not converge for site MSH, where the Arai plots were so non linear, with  
 865 few points, that BiCEP struggled to fit circles to them. We consider these sites to have  
 866 “failed” using our method (grade of ‘D’ in Figure 9) and use the prior distribution on  
 867  $B_{anc}$  (uniform between 0 and 250  $\mu\text{T}$ ) as an estimate of their intensity. We calculate the  
 868  $\hat{R}$  furthest from unity, the  $n_{eff}$  for  $B_{anc}$  and the proportion of divergent samples  $f_{div}$   
 869 for our model.

## 870 6.3 Code and GUI

871 We present a simple GUI that can perform the BiCEP method on data in the MagIC  
 872 format. The code uses Jupyter notebooks and can be found at ([http://github.com/  
 873 bcych/BiCEP\\_GUI](http://github.com/bcych/BiCEP_GUI)) and contains a readme file detailing how to use the notebook. The  
 874 GUI can also be accessed at the Earthref JupyterHub site ([http://jupyterhub.earthref  
 875 .org](http://jupyterhub.earthref.org)). To access the GUI this way:

- 876 • Sign up to Earthref at (<http://earthref.org>)
- 877 • Navigate to the Earthref JupyterHub site at (<http://jupyterhub.earthref.org>)
- 878 • Open and run all the cells in the “BiCEP GUI - Setup.ipynb” notebook.

- 879 • Upload MagIC formatted “sites”, “samples”, “specimens” and “measurements”  
880 files to the BiCEP\_GUI directory in JupyterHub. These can be formatted using  
881 pmag\_gui (Tauxe et al., 2016).
- 882 • Open the BiCEP GUI notebook and press the “App Mode” button.

883 For more detailed instructions, read the included readme file at the github site.

## 884 Acknowledgments

885 We are deeply grateful to Lennart de Groot and Greig Paterson for their very helpful  
886 reviews and for the advice and guidance given by Andrew Roberts, David Heslop and  
887 Joseph Wilson. This research was supported in part by NSF Grant EAR1827263 to LT.  
888 We are also grateful to Agnes Lisé-Pronovost for sharing her measurement level data for  
889 use in section 4.6.

## 890 References

- 891 Biggin, A. J. (2010). Paleointensity database updated and upgraded. *EOS*, *91*, 15.
- 892 Biggin, A. J., Perrin, M., & Dekkers, M. J. (2007). A reliable absolute palaeoin-  
893 tensity determination obtained from a non-ideal recorder. *Earth and Planetary*  
894 *Science Letters*, *257*(3), 545-563. doi: <https://doi.org/10.1016/j.epsl.2007.03>  
895 .017
- 896 Bowles, J., Gee, J. S., Kent, D. V., Perfit, M. R., Soule, S. A., & Fornari, D. J.  
897 (2006). Paleointensity applications to timing and extent of eruptive activity,  
898 9°–10°n east pacific rise. *Geochemistry, Geophysics, Geosystems*, *7*(6). doi:  
899 <https://doi.org/10.1029/2005GC001141>
- 900 Chernov, N., & Lesort, C. (2005). Least squares fitting of circles. *Journal of Mathe-*  
901 *matical Imaging and Vision*, *23*(3), 239–252. doi: 10.1007/s10851-005-0482-8
- 902 Cromwell, G., Tauxe, L., Staudigel, H., & Ron, H. (2015). Paleointensity esti-  
903 mates from historic and modern hawaiian lava flows using glassy basalt  
904 as a primary source material. *Phys. Earth Planet. Int.*, *241*, 44–56. doi:  
905 10.1016/j.pepi.2014.12.007
- 906 Donadini, F., Kovacheva, M., Kostadinova, M., Casas, L., & Pesonen, L. (2007).  
907 New archaeointensity results from scandinavia and bulgaria: Rock-magnetic  
908 studies inference and geophysical application. *Physics of the Earth and*  
909 *Planetary Interiors*, *165*(3), 229-247. doi: [https://doi.org/10.1016/j](https://doi.org/10.1016/j.pepi.2007.10.002)  
910 [pepi.2007.10.002](https://doi.org/10.1016/j.pepi.2007.10.002)
- 911 Dunlop, D., & Özdemir, O. (2001). Beyond Néel’s theories: thermal demagnetization  
912 of narrow-band partial thermoremanent magnetization. *Phys. Earth Planet.*  
913 *Int.*, *126*, 43-57.
- 914 Gelman, A., Carlin, J. B., Stern, H. S., & Rubin, D. B. (2004). *Bayesian data analy-*  
915 *sis* (Second ed.). Chapman & Hall/CRC, Boca Raton, FL.
- 916 Gelman, A., & Rubin, D. B. (1992, 11). Inference from iterative simulation using  
917 multiple sequences. *Statist. Sci.*, *7*(4), 457–472. doi: 10.1214/ss/1177011136
- 918 Hoffman, K. A., Constantine, V. L., & Morse, D. L. (1989). Determinaton of abso-  
919 lute palaeointensity using a multi-specimen procedure. *Nature*, *339*, 295-297.
- 920 Königsberger, J. G. (1938). Natural residual magnetism of eruptive rocks. *Ter-*  
921 *restrial Magnetism and Atmospheric Electricity*, *43*(3), 299-320. doi: 10.1029/  
922 TE043i003p00299
- 923 Korte, M., Donadini, F., & Constable, C. G. (2009). Geomagnetic field for 0–3 ka: 2.  
924 a new series of time-varying global models. *Geochemistry, Geophysics, Geosys-*  
925 *tems*, *10*(6). doi: <https://doi.org/10.1029/2008GC002297>
- 926 Kosareva, L. R., Kuzina, D. M., Nurgaliev, D. K., Sitdikov, A. G., Luneva, O. V.,  
927 Khasanov, D. I., . . . Spassov, S. (2020). Archaeomagnetic investiga-

- 928 tions in Bolgar (Tatarstan). *Stud. Geophys. Geod.*, *64*(2), 255–292. doi:  
929 10.1007/s11200-019-0493-3
- 930 Krása, D., Heunemann, C., Leonhardt, R., & Petersen, N. (2003). Experimental  
931 procedure to detect multidomain remanence during thellier–thellier experi-  
932 ments. *Phys. Chem Earth (A/B/C)*, *28*(16), 681–687. (Paleo, Rock and  
933 Environmental Magnetism 2002) doi: 10.1016/S1474-7065(03)00122-0
- 934 Lisé-Pronovost, A., Mallett, T., & Herries, A. I. R. (2020). Archaeointensity of  
935 nineteenth-century scottish firebricks from a foundry in melbourne, australia:  
936 comparisons with field models and magnetic observatory data. *Geological Soci-  
937 ety, London, Special Publications*, *497*(1), 27–45. doi: 10.1144/SP497-2019-72
- 938 Muxworthy, A. R., Heslop, D., Paterson, G. A., & Michalk, D. (2011). A preisach  
939 method for estimating absolute paleofield intensity under the constraint of  
940 using only isothermal measurements: 2. experimental testing. *Journal of  
941 Geophysical Research: Solid Earth*, *116*(B4). doi: [https://doi.org/10.1029/  
942 2010JB007844](https://doi.org/10.1029/2010JB007844)
- 943 Nagata, T., Arai, Y., & Momose, K. (1963). Secular variation of the geomagnetic to-  
944 tal force during the last 5000 years. *J. Geophys. Res.*, *68*(18), 5277–5281. doi:  
945 10.1029/j.2156-2202.1963.tb00005.x
- 946 Nagy, L., Williams, W., Muxworthy, A. R., Fabian, K., Almeida, T. P., Conbhuí,  
947 P. Ó., & Shcherbakov, V. P. (2017). Stability of equidimensional pseudo-  
948 single-domain magnetite over billion-year timescales. *Proc. Natl. Acad. Sci.  
949 U.S.A.*, *114*(39), 10356–10360. doi: 10.1073/pnas.1708344114
- 950 Néel, L. (1949). Théorie du traînage magnétique des ferromagnétiques en grains fins  
951 avec applications aux terres cuites. *Ann. géophys.*, *5*, 99–136.
- 952 Paterson, G. A. (2011). A simple test for the presence of multidomain be-  
953 havior during paleointensity experiments. *J. Geophys. Res.*, *116*. doi:  
954 10.1029/2011JB008369
- 955 Paterson, G. A., Biggin, A. J., Yamamoto, Y., & Pan, Y. (2012). Towards the ro-  
956 bust selection of Thellier-type paleointensity data: The influence of experimen-  
957 tal noise. *Geochem. Geophys. Geosyst.*, *13*(5). doi: 10.1029/2012GC004046
- 958 Paterson, G. A., Muxworthy, A. R., Roberts, A. P., & Mac Niocaill, C. (2010).  
959 Assessment of the usefulness of lithic clasts from pyroclastic deposits for pa-  
960 leointensity determination. *Journal of Geophysical Research: Solid Earth*,  
961 *115*(B3). doi: <https://doi.org/10.1029/2009JB006475>
- 962 Paterson, G. A., Tauxe, L., Biggin, A. J., Shaar, R., & Jonestrask, L. C. (2014). On  
963 improving the selection of thellier-type paleointensity data. *Geochem. Geophys.  
964 Geosyst.*, *15*(4), 1180–1192. doi: 10.1002/2013GC005135
- 965 Pick, T., & Tauxe, L. (1993). Holocene paleointensities: Thellier experiments on  
966 submarine basaltic glass from the east pacific rise. *Journal of Geophysical  
967 Research: Solid Earth*, *98*(B10), 17949–17964. doi: [https://doi.org/10.1029/  
968 93JB01160](https://doi.org/10.1029/93JB01160)
- 969 Santos, C. N., & Tauxe, L. (2019). Investigating the accuracy, precision, and cooling  
970 rate dependence of laboratory-acquired thermal remanences during paleoin-  
971 tensity experiments. *Geochem., Geophys., Geosyst.*, *20*(1), 383–397. doi:  
972 10.1029/2018GC007946
- 973 Shaar, R., Ron, H., Tauxe, L., Kessel, R., & Agnon, A. (2011). Paleomagnetic field  
974 intensity derived from non-sd: Testing the thellier izzi technique on md slag  
975 and a new bootstrap procedure. *Earth and Planetary Science Letters*, *310*(3),  
976 213–224. doi: <https://doi.org/10.1016/j.epsl.2011.08.024>
- 977 Shaar, R., Ron, H., Tauxe, L., Kessel, R., Agnon, A., Ben-Yosef, E., & Feinberg,  
978 J. M. (2010). Testing the accuracy of absolute intensity estimates of the  
979 ancient geomagnetic field using copper slag material. *Earth and Planetary Sci-  
980 ence Letters*, *290*(1), 201–213. doi: <https://doi.org/10.1016/j.epsl.2009.12.022>
- 981 Shaar, R., & Tauxe, L. (2013). Thellier\_gui: An integrated tool for analyzing pa-  
982 leointensity data from thellier-type experiments. *Geochem. Geophys. Geosys.*,

- 983 14, 677–692. doi: doi:10.1002/ggge.20062
- 984 Shaw, J. (1974). A new method of determining the magnitude of the paleomagnetic  
985 field application to 5 historic lavas and five archeological samples. *Geophys. J.*  
986 *R. astr. Soc.*, 39, 133-141.
- 987 Tanaka, H., Hashimoto, Y., & Morita, N. (2012, 05). Palaeointensity determina-  
988 tions from historical and Holocene basalt lavas in Iceland. *Geophysical Journal*  
989 *International*, 189(2), 833-845. doi: 10.1111/j.1365-246X.2012.05412.x
- 990 Tauxe, L., Santos, C., Cych, B., Zhao, X., Roberts, A., Nagy, L., & Williams, W.  
991 (2021). Understanding non-ideal paleointensity recording in igneous rocks:  
992 Insights from aging experiments on lava samples and the causes and conse-  
993 quences of 'fragile' curvature in arai plots. *Geochem. Geophys. Geosyst.*, 22,  
994 e2020GC009423. doi: 10.1029/2020GC009423
- 995 Tauxe, L., Shaar, R., Jonestrask, L., Swanson-Hysell, N. L., Minnett, R., Koppers,  
996 A. a. P., ... Fairchild, L. (2016). PmagPy: Software package for paleomag-  
997 netic data analysis and a bridge to the magnetism information consortium  
998 (MagIC) database. *Geochem., Geophys., Geosyst.*, 17(6), 2450–2463. doi:  
999 10.1002/2016GC006307
- 1000 Tauxe, L., & Yamazaki, T. (2015). Paleointensities. In M. Kono (Ed.), *Geomag-*  
1001 *netism* (2nd Edition ed., Vol. 5, p. 461-509). Elsevier.
- 1002 Thébaud, E., Finlay, C. C., Beggan, C. D., Alken, P., Aubert, J., Barrois, O., ...  
1003 Zvereva, T. (2015). International Geomagnetic Reference Field: the 12th  
1004 generation. *Earth Planets Space*, 67(1), 79. doi: 10.1186/s40623-015-0228-9
- 1005 Thellier, E., & Thellier, O. (1959). Sur l'intensité du champ magnétique terrestre  
1006 dans le passé historique et géologique. *Ann. Geophys.*, 15, 285.
- 1007 Valet, J.-P., Brassart, J., Le Meur, I., Soler, V., Quidelleur, X., Tric, E., & Gillot,  
1008 P.-Y. (1996). Absolute paleointensity and magnetomineralogical changes.  
1009 *Journal of Geophysical Research: Solid Earth*, 101(B11), 25029-25044. doi:  
1010 <https://doi.org/10.1029/96JB02115>
- 1011 Williams, W., & Dunlop, D. J. (1989). Three-dimensional micromagnetic modelling  
1012 of ferromagnetic domain structure. *Nature*, 337, 634–637.
- 1013 Yamamoto, Y., & Hoshi, H. (2008). Paleomagnetic and rock magnetic studies of  
1014 the sakurajima 1914 and 1946 andesitic lavas from japan: A comparison of  
1015 the ltd-dht shaw and thellier paleointensity methods. *Phys. Earth and Planet.*  
1016 *Inter.*, 167, 118-143.
- 1017 Yamamoto, Y., Tsunakawa, H., & Shibuya, H. (2003). Palaeointensity study of  
1018 the hawaiian 1960 lava: implications for possible causes of erroneously high  
1019 intensities. *Geophys J Int*, 153(1), 263-276.
- 1020 Yamamoto, Y., & Yamaoka, R. (2018). Paleointensity study on the Holocene surface  
1021 lavas on the Island of Hawaii using the Tsunakawa-Shaw method. *Front. Earth*  
1022 *Sci.*, 6. doi: 10.3389/feart.2018.00048
- 1023 Yu, Y., Tauxe, L., & Genevey, A. (2004). Toward an optimal geomagnetic field in-  
1024 tensity determination technique. *Geochem., Geophys., Geosyst.*, 5(2). doi: 10  
1025 .1029/2003GC000630

# Supporting Information for “Bias Corrected Estimation of Paleointensity (BiCEP): An improved methodology for obtaining paleointensity estimates”

Brendan Cych<sup>1</sup>, Matthias Morzfeld<sup>1</sup>, Lisa Tauxe<sup>1</sup>

<sup>1</sup>University of California, San Diego

<sup>1</sup>9500 Gilman Drive, La Jolla, CA, 92093, USA

## Contents of this file

1. Figure S1- plots of  $B_{exp}$  vs  $B_{anc}$  results using the BiCEP method and other sets of selection criteria used in this study.
2. Figure S2- plots of the credible intervals of BiCEP results for subsamples of 5 specimens from sites hw108, VM and hw123.
3. Figures S3 to S32- plots of unpooled  $B_{anc}$  and  $\vec{k}$  fits and the BiCEP method applied to all sites used in this study.

## Additional Supporting Information (Files uploaded separately)

1. Caption for Data Set S1 - This dataset contains the full set of results shown in Figure 7 and described in Section 3.

## Data Set S1

This data set is a csv file containing the full set of results for each version of the BiCEP method (Linear, Quadratic and Cubic models with 5, 10 and 20  $\mu$ T standard deviations

---

on the prior for  $\sigma_{site}$ , vs classic selection criteria. Columns are named by the model class (Linear, Quadratic, Cubic, or Selection Criteria, followed by the criteria name/prior standard deviation in  $\mu\text{T}$ ) and then the parameter in question, either the percentile (2.5%, 50%, 97.5%) or  $f_{prob}$  for the  $f_{prob}$  value. The first three columns of the csv file contain the site name,  $B_{exp}$  and number of specimens (M).

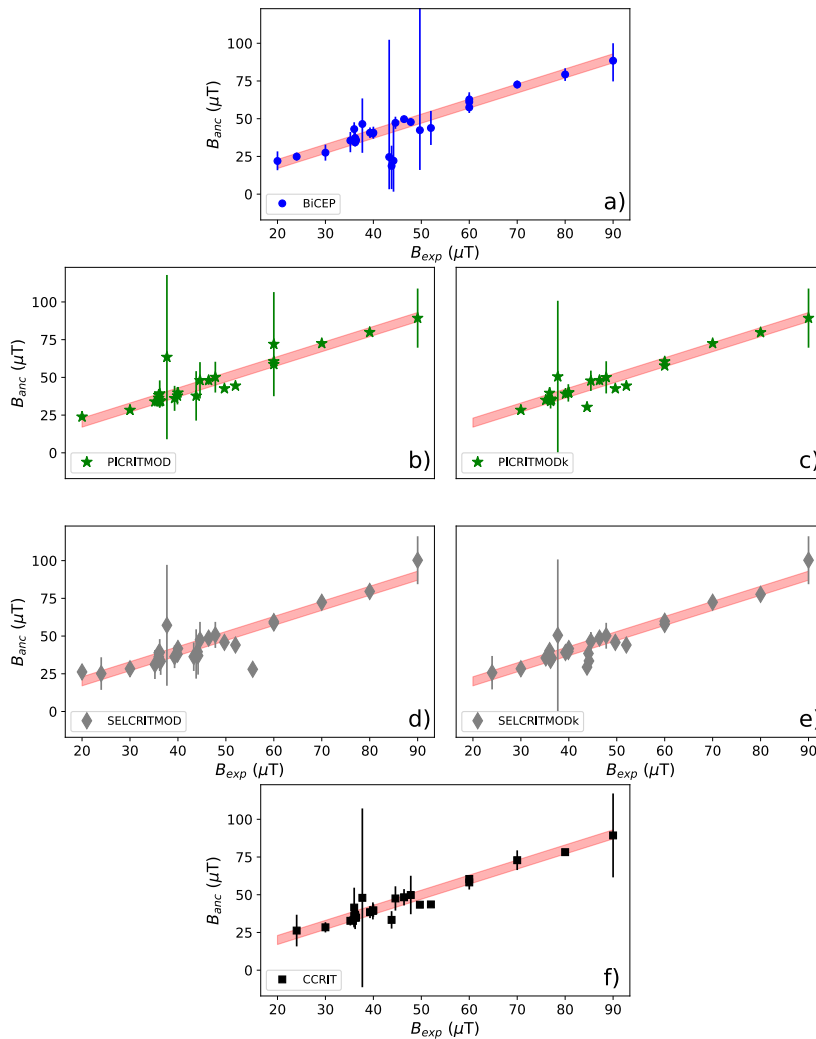


**Figure S1.** Plot of  $B_{anc}$  vs  $B_{exp}$  for the passing sites for BiCEP and each of our criteria. a) BiCEP results, b) PICCRITMOD results, c) PICRITMODk results, d) SELCRIT results, e) SELCRITMODk results, f) CCRIT results. Red shaded area represents  $B_{exp} \pm 3 \mu\text{T}$ . Note that for BiCEP, most of the severely underestimated and highly inaccurate results are for sites with low numbers of specimens ( $M < 5$ ) which did not pass the other criteria.

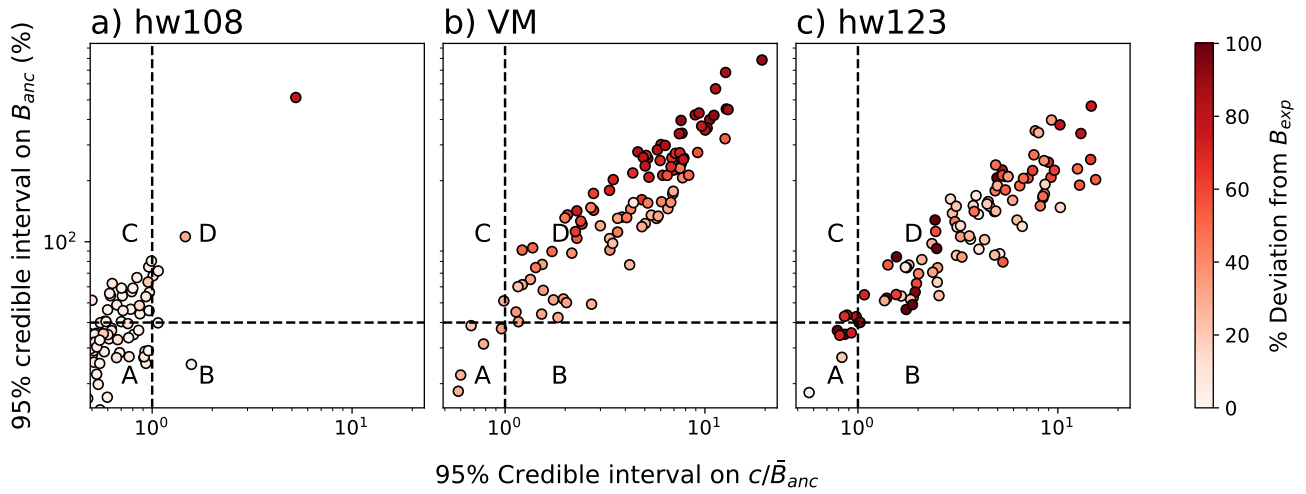


**Figure S2.** Figure in the style of Figure 9 from the main manuscript. A set of 100 random subsamples of 5 specimens were taken from a) site hw108, b) site VM and c) site hw123. We applied the BiCEP method to these subsamples and plot the 95% credible interval on  $B_{anc}$  as a percentage against the 95% credible interval on  $c/\tilde{B}_{anc}$ . Dashed lines represent the boundaries between regions A, B, C and D, defined in Section 4.3, and point colors represent the percentage deviation of the median from  $B_{exp}$ . It is apparent that for our sites where we obtain an inaccurate answer for a large number of specimens (VM and hw123), our subsamples fall in region D the majority of the time (94/100 and 90/100 respectively). Conversely, our site hw108, which returns an accurate result with higher numbers of specimens only has 5 results in region D. This indicates that we should either continue measuring specimens (region C, 24/100 results) or that we have a relatively accurate and precise result already (regions A and B, 66/100 results). Although few sites/subsamples were used for this analysis, this test indicates that our labelling scheme has a predictive accuracy of 90-95%

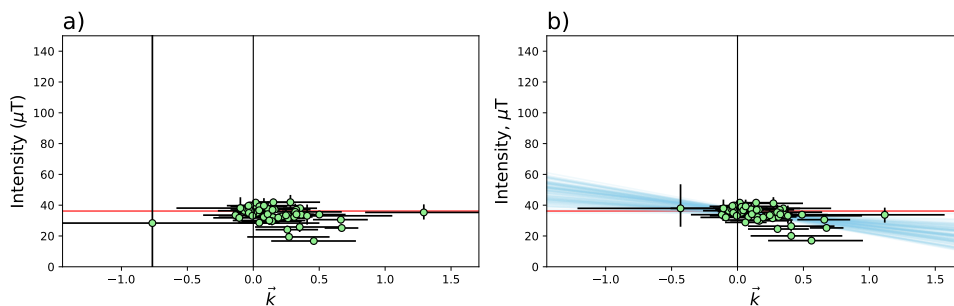


**Figure S3.** Unpooled and BiCEP models applied to site 1991-1992 Eruption Site a). Independent estimates of  $B_{anc}$  vs  $\vec{k}$  are plotted as green circles. These estimates are made without assuming a linear relationship between  $B_{anc}$  and  $\vec{k}$ , similar to the analysis in Figure 9a) Black error bars represent 95% credible intervals. b) The BiCEP method applied to this site. Green circles and error bars represent the 95% credible interval, blue lines represent draws from the posterior distribution. The  $\vec{k}=0$  axis is plotted as a black vertical line, and the value of  $B_{exp}$  is plotted as a red horizontal line. For an accurate estimate, the blue lines should cross the point where these two lines intersect.

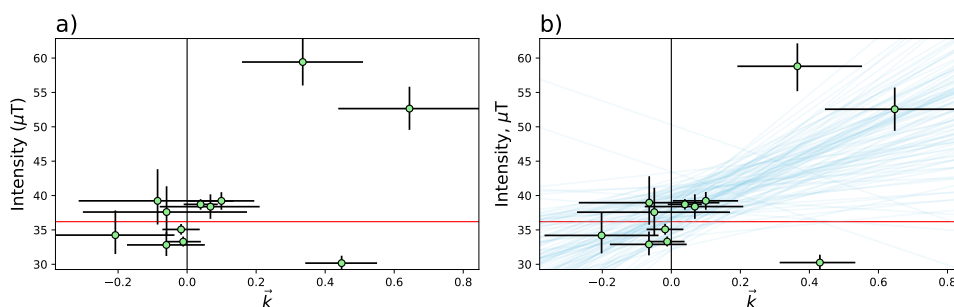


**Figure S4.** The same methodology described in the caption for Figure S3 applied to site BBQ

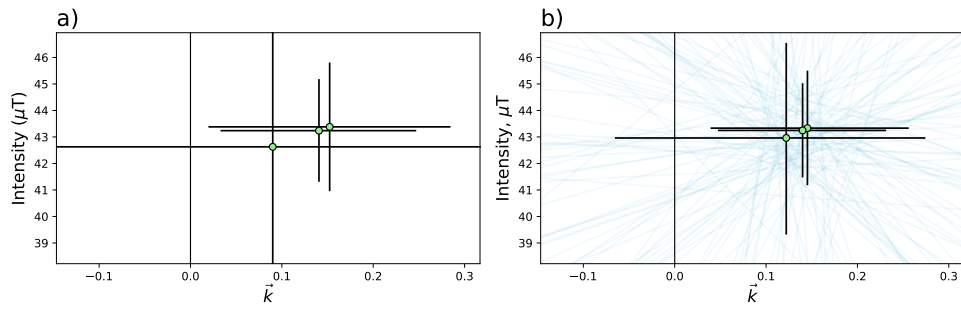


**Figure S5.** The same methodology described in the caption for Figure S3 applied to site BR06

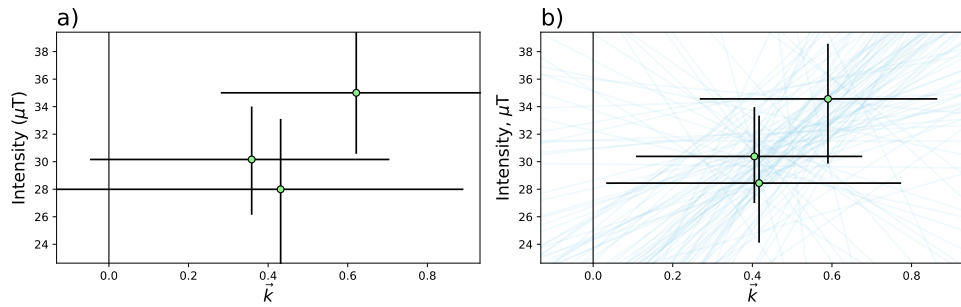


**Figure S6.** The same methodology described in the caption for Figure S3 applied to site ET1

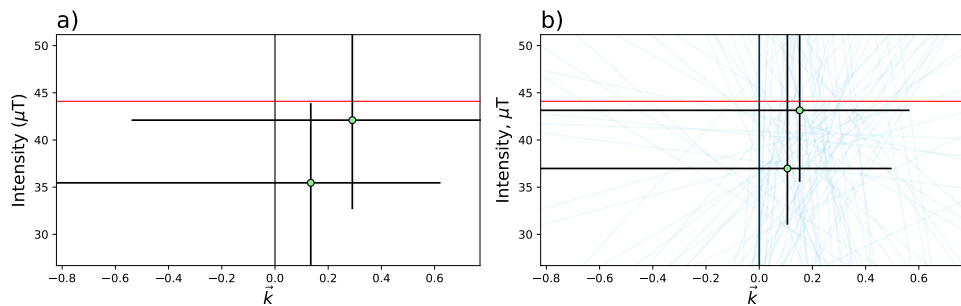


**Figure S7.** The same methodology described in the caption for Figure S3 applied to site ET2

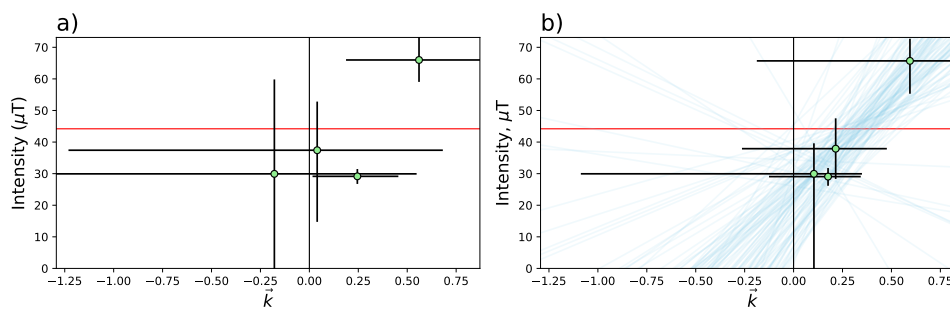


**Figure S8.** The same methodology described in the caption for Figure S3 applied to site ET3

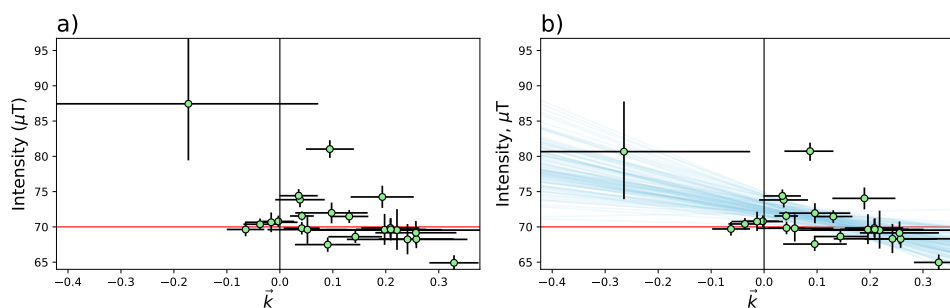


**Figure S9.** The same methodology described in the caption for Figure S3 applied to site FreshTRM

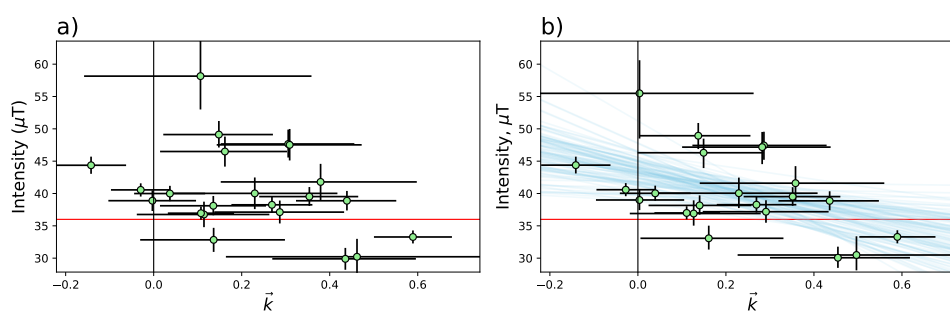


**Figure S10.** The same methodology described in the caption for Figure S3 applied to site Hawaii 1960 Flow

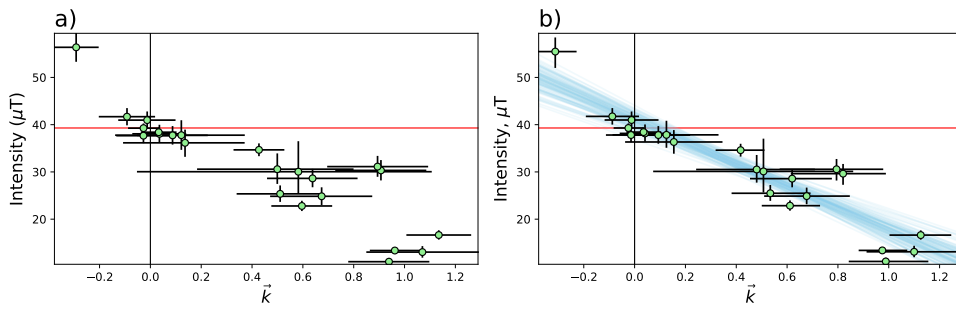


**Figure S11.** The same methodology described in the caption for Figure S3 applied to site hw108

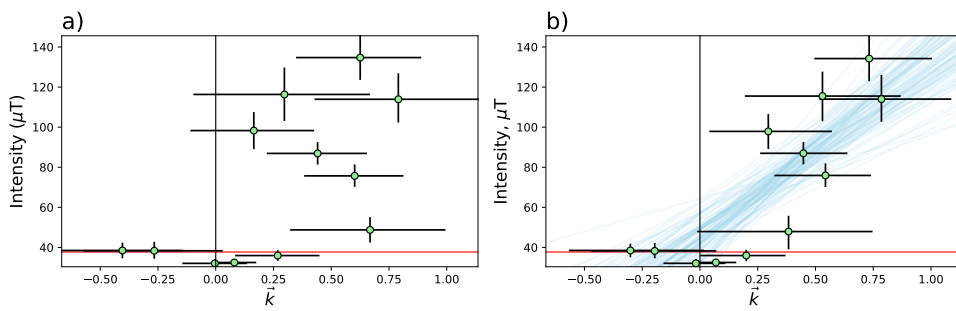


**Figure S12.** The same methodology described in the caption for Figure S3 applied to site hw123

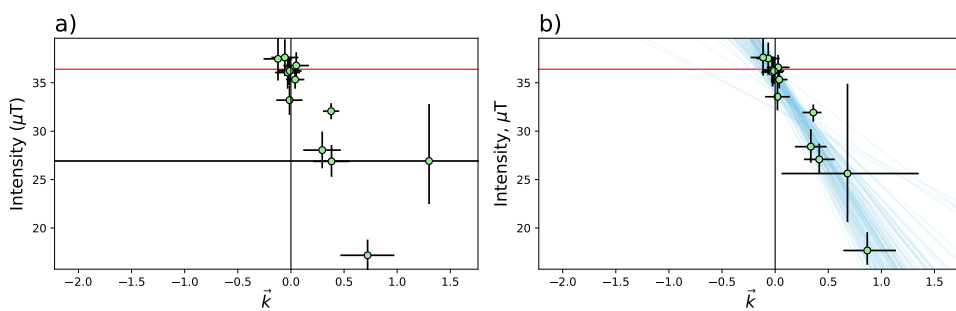


**Figure S13.** The same methodology described in the caption for Figure S3 applied to site hw126

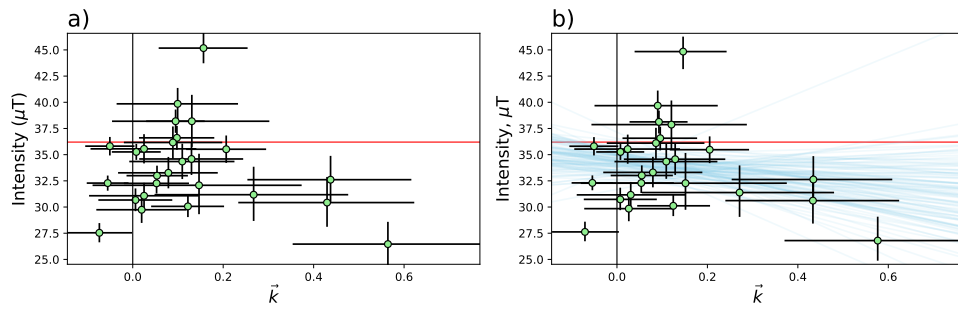


**Figure S14.** The same methodology described in the caption for Figure S3 applied to site hw128

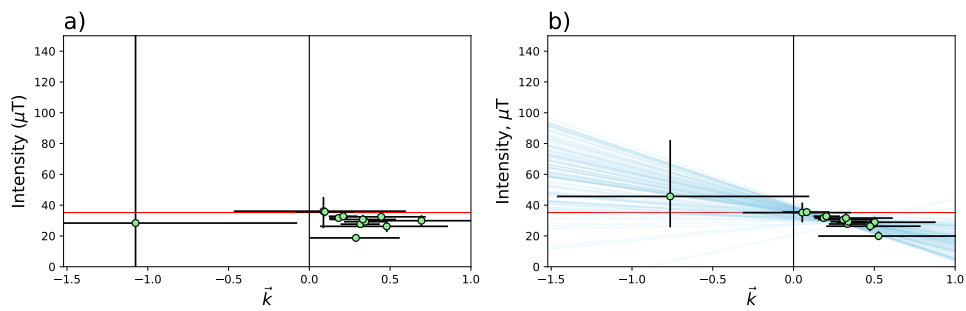


**Figure S15.** The same methodology described in the caption for Figure S3 applied to site hw201

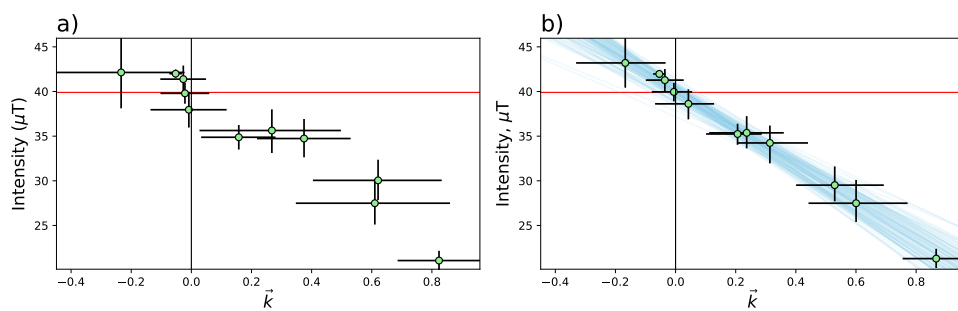


**Figure S16.** The same methodology described in the caption for Figure S3 applied to site hw226

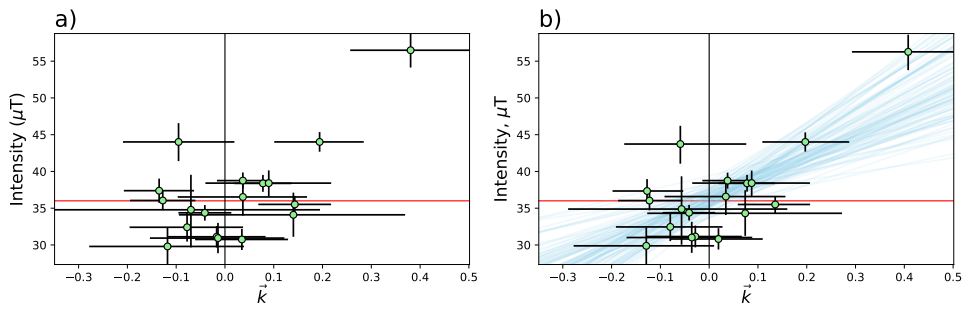


**Figure S17.** The same methodology described in the caption for Figure S3 applied to site hw241

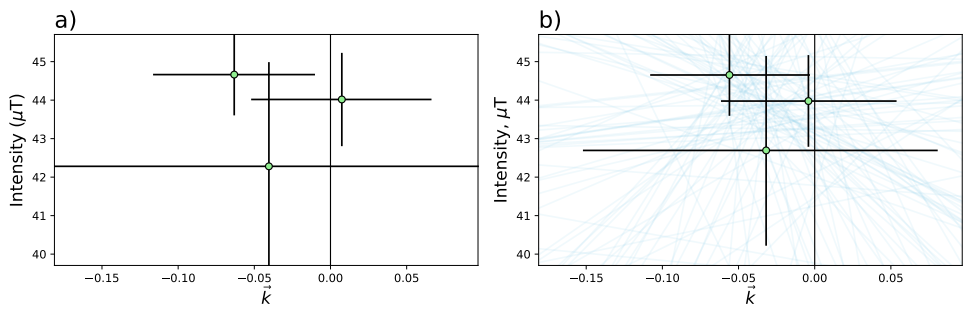


**Figure S18.** The same methodology described in the caption for Figure S3 applied to site kf

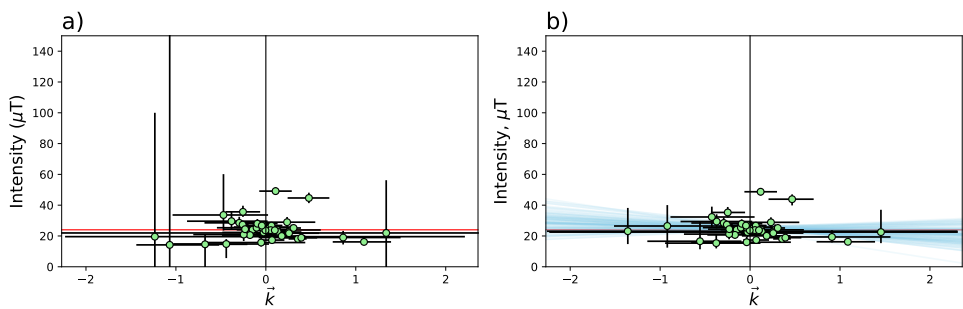


**Figure S19.** The same methodology described in the caption for Figure S3 applied to site LV

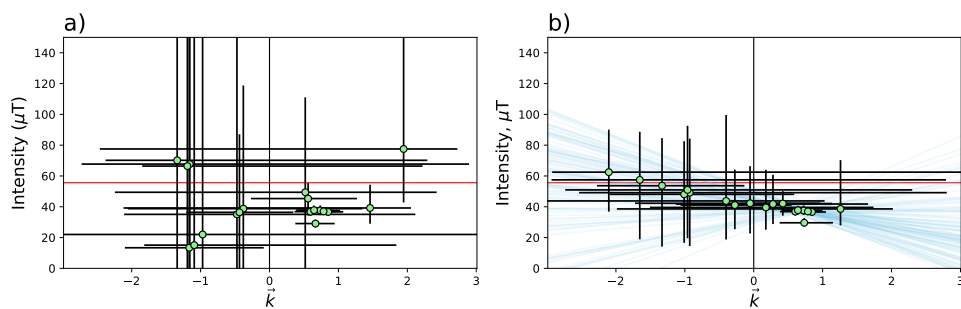


**Figure S20.** The same methodology described in the caption for Figure S3 applied to site MSH

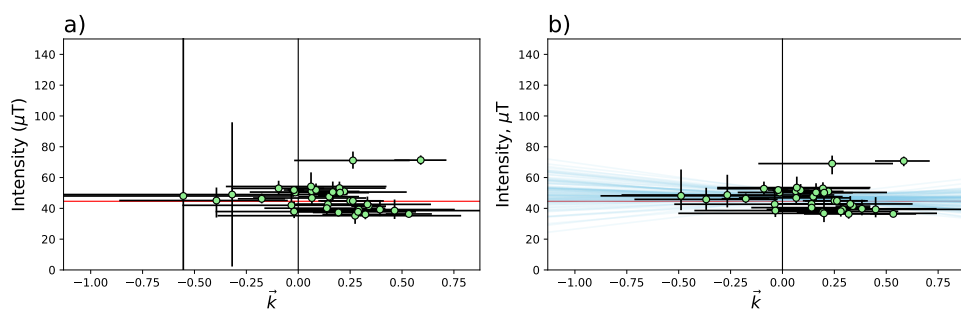


**Figure S21.** The same methodology described in the caption for Figure S3 applied to site P

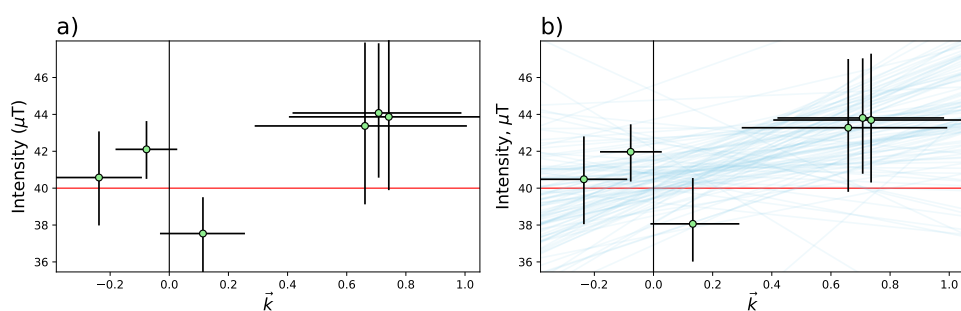


**Figure S22.** The same methodology described in the caption for Figure S3 applied to site remag-rs61

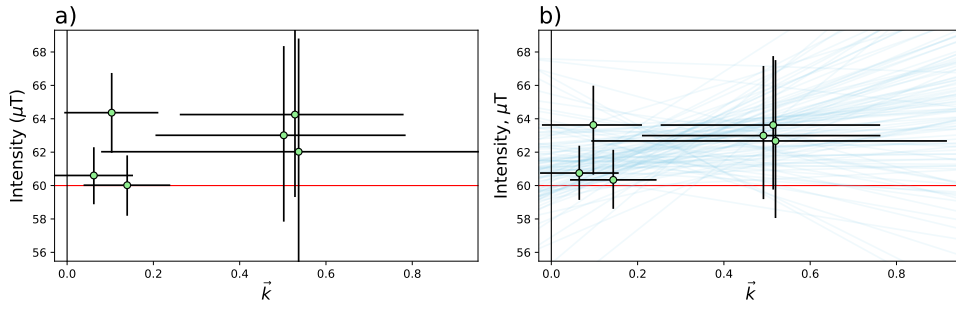


**Figure S23.** The same methodology described in the caption for Figure S3 applied to site remag-rs62

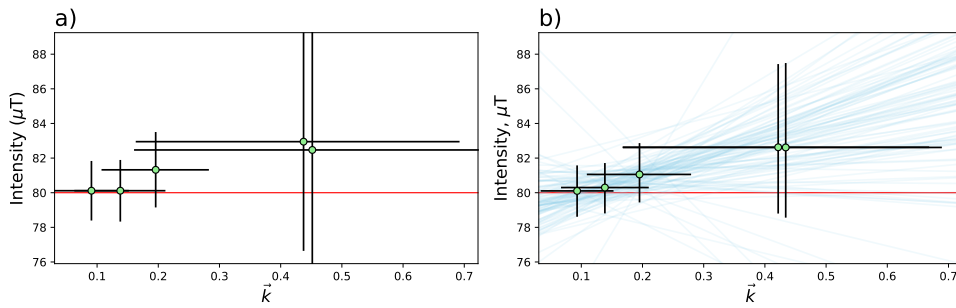


**Figure S24.** The same methodology described in the caption for Figure S3 applied to site remag-rs63

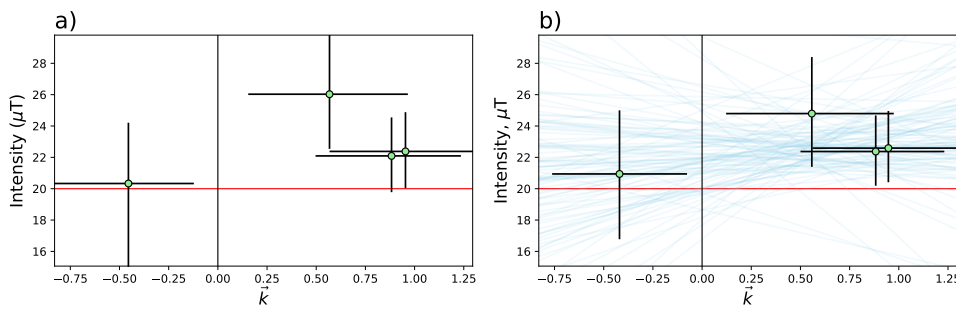


**Figure S25.** The same methodology described in the caption for Figure S3 applied to site remag-rs78

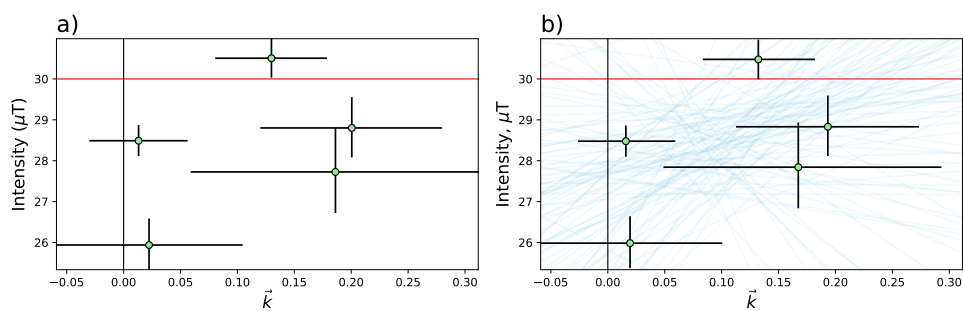


**Figure S26.** The same methodology described in the caption for Figure S3 applied to site rs25

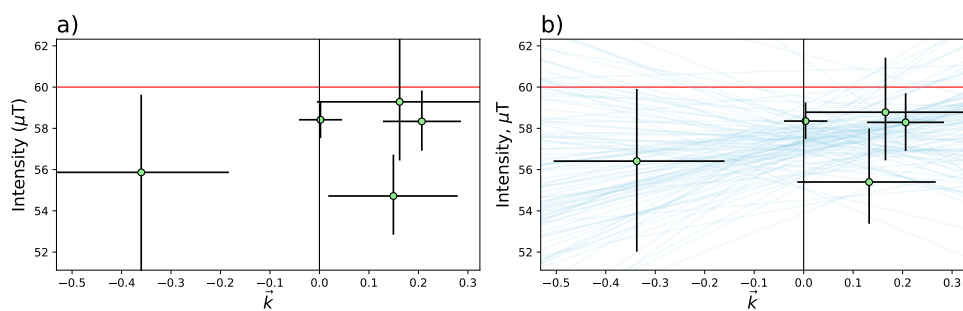


**Figure S27.** The same methodology described in the caption for Figure S3 applied to site rs26

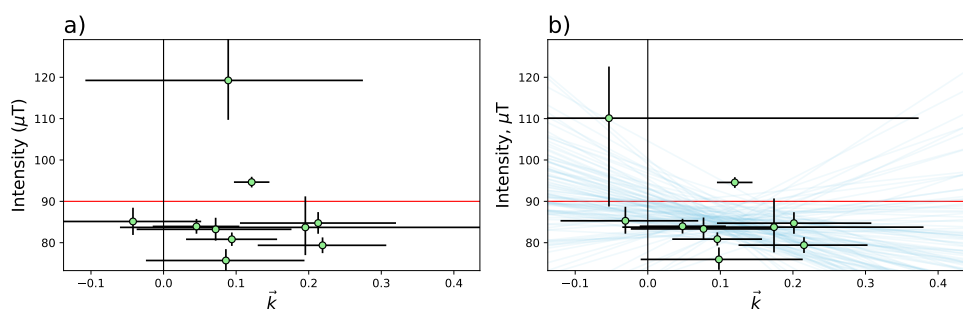


**Figure S28.** The same methodology described in the caption for Figure S3 applied to site rs27

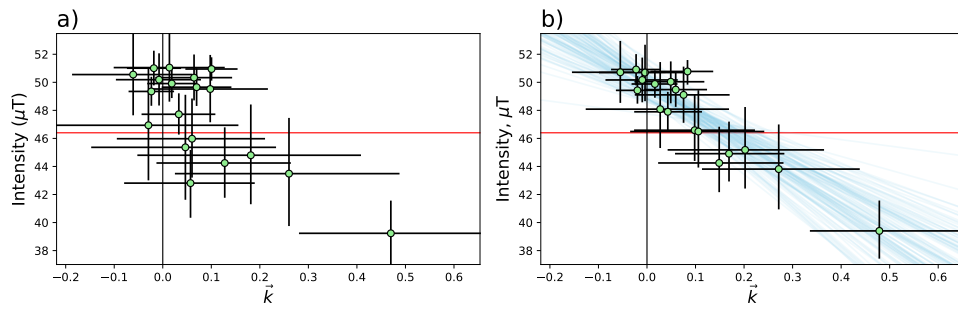


**Figure S29.** The same methodology described in the caption for Figure S3 applied to site SW

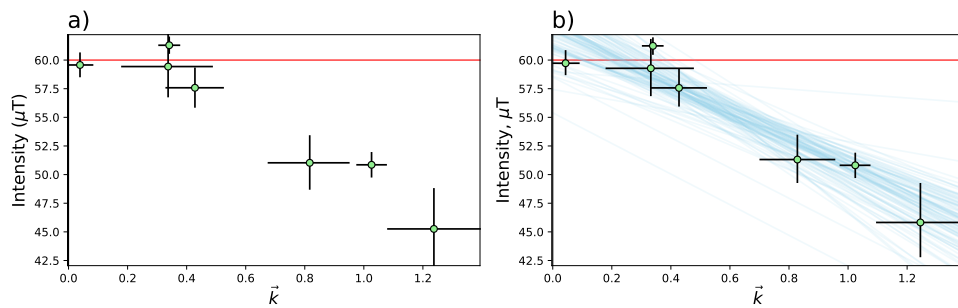


**Figure S30.** The same methodology described in the caption for Figure S3 applied to site Synthetic60

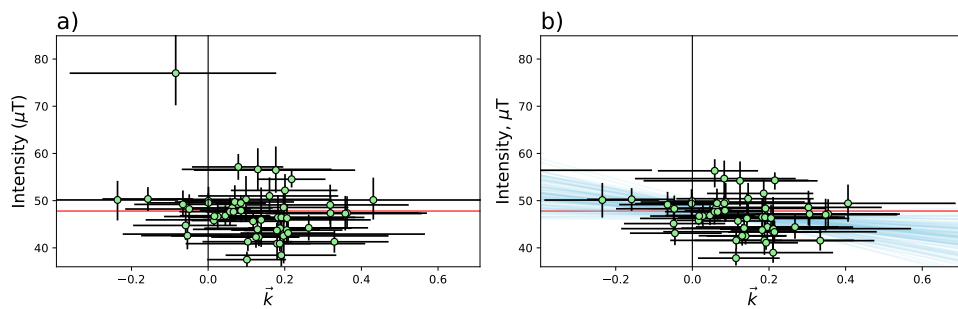


**Figure S31.** The same methodology described in the caption for Figure S3 applied to site TS

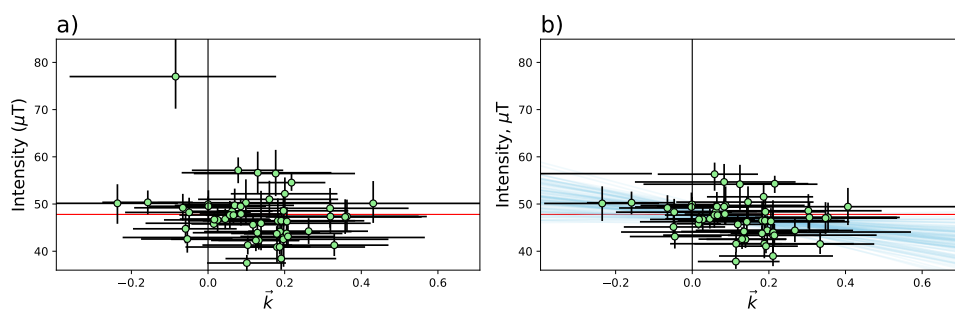


**Figure S32.** The same methodology described in the caption for Figure S3 applied to site VM